8-2010

Parametric Instabilities for Vibratory Energy Harvesting under Harmonic, Time-Varying Frequency, and Random Excitations

Christopher Stabler
Clemson University, stabler.chris@gmail.com

PARAMETRIC INSTABILITIES FOR VIBRATORY ENERGY HARVESTING UNDER HARMONIC, TIME-VARYING FREQUENCY, AND RANDOM EXCITATIONS

A Thesis

Presented to

the Graduate School of

Clemson University

In Partial Fulfillment

of the Requirements for the Degree

Master of Science

Mechanical Engineering

---

by

Christopher Stabler

August 2010

Accepted by:

Mohammed F. Daqaq, Committee Chair

Georges Fadel

John Wagner

ABSTRACT

This effort investigates and evaluates the prospect of using *parametric instabilities* for vibratory energy harvesting. To that end, we consider a parametrically-excited piezoelectric cantilever beam and study its performance as an energy harvester under *i*) fixed-frequency harmonic excitations, *ii*) time-varying frequency excitations, and *iii*) band-limited Gaussian noise. In the case of fixed-frequency excitations, we use the Method of Multiple Scales to obtain approximate analytical expressions for the steady-state response amplitude and instantaneous output power in the vicinity of the first *principle parametric resonance*. We show that the electromechanical coupling and load resistance play an important role in determining the output power and characterizing the bandwidth of the harvester. Specifically, we demonstrate that the region of parametric instability wherein energy can be harvested shrinks as the coupling coefficient increases, and that there exists a coupling coefficient beyond which the peak power decreases. We also show that there is a critical excitation level below which no energy can be harvested. The magnitude of this critical excitation increases with the coupling coefficient and is maximized for a given electric load resistance. Theoretical findings were compared to experimental data showing good agreement and reflecting the general physical trends.

In the case of time-varying frequency excitations, we consider two beams of different nonlinear behaviors: one exhibiting a *softening* response while the other exhibiting *hardening* characteristics. We show that, for both beams, the bandwidth of the harvester decreases with increasing frequency sweep rate and that the instantaneous peak power during a sweep cycle decreases and shifts in the direction of the sweep. Furthermore, experimental findings illustrate that the average output power of the harvester is significantly higher when the sweep is in the direction in which the steady-state principle parametric resonance curves of the beams bend. Also, as the frequency sweep rate increases, the average output power decreases until beyond a

threshold sweep rate where no power can be harvested.

Based on the preceding conclusions, we introduce the new concept of a Softening-Hardening Hysteretic Harvester (SHHH), which is designed to scavenge energy efficiently from an excitation source whose frequency varies with time around a center frequency. Introductory experimental investigation on the SHHH illustrated that this concept produces more power than either a softening or a hardening beam alone.

Finally, in an effort to duplicate real-world scenarios under which energy harvesting occurs, both the hardening and the softening beam were subjected to parametric, band-limited, random Gaussian excitations and their performance in scavenging energy under different excitation bandwidths was evaluated. We observed that, under narrow bandwidth excitations (on the order of the harvester's steady-state bandwidth) and regardless of the beam's nonlinear characteristics, the parametric instability was activated for the length of the experiment. However, the average output power was very low (on the order of micro-Watts under excitations having a variance of 1.5 g). The power decreased even further as the bandwidth of the excitation was increased.

Dedication

To my parents, Bill and Donna.

Their love and support have made this work possible.

Acknowledgments

First, I would like to thank the Lord, who brought me to Clemson and has guided me to this point, for His many blessings, gentle patience, and ever present love.

Secondly, I thank Mom, Dad, and Greg for their love and support during my time in graduate school and their encouragement to succeed.

Also, I thank my soon-to-be wife, Meredith, for her encouragement, patience, and love while I finished. I look forward to our new life together.

I also thank my CP Group from CrossPoint for their many prayers on my behalf as I worked to finish and their wonderful fellowship over the past two years. They are, each, salt and light.

I thank my good friend and advisor, Dr. Mohammed Daqaq. You have been patient, encouraging, and willing to teach from the first day I started work in your lab. I have learned a tremendous amount from you, both about dynamics and life. It has been a privilege to study under you; thank you for your friendship and dedication.

I thank my committee members, Dr. Georges Fadel and Dr. John Wagner, for their help and willingness to serve on my committee.

I also thank Dr. Todd Schweisinger for giving me the opportunity to be a Teaching Assistant for ME 222 and for his great friendship. It was an experience that I will not soon forget and I am grateful to have had it.

Finally, I thank my fellow office mates, especially Amin, Yousef, Ravindra, Clodoaldo, Tugba, Thiago, and Keyur. It has been a joy to get to know each of you and to learn about your customs and cultures. My horizons have truly been broadened; I will miss our conversations.

Contents

List of Figures

List of Tables

Chapter 1

Introduction

1.1 Background

Energy harvesting is the process of capturing ambient energy in an environment and utilizing it to power some process. Historically, energy harvesting has been practiced in the form of windmills, sailing ships, and waterwheels. It was not until the invention of the steam engine that man had a reliable source of energy that was not captured from the environment. Today, the world is primarily powered by energy generated from the combustion of fossil fuels. Energy harvesting is still used to provide power from solar, wind, and geothermal sources, but contemporary research is taking an old concept in a new direction. Currently, energy harvesting is being investigated as a replacement for batteries.

Current energy needs and research trends have taken the old concept of energy harvesting in a new direction. Today, researchers have developed new devices that can transform mechanical motions directly into electricity via a process known as *vibration-based energy harvesting*. This new concept exploits the ability of active materials and some electromechanical mechanisms to generate an electric potential

in response to mechanical stimuli or external stresses, giving rise to the potential for *ad hoc* energy sources [1, 2, 3].

Vibratory energy harvesting has attracted significant interest due to critical advances in manufacturing electronics and in computational fields that made low-power consumption devices a reality. For instance, many critical electronic devices, such as health-monitoring sensors [4, 5], pace makers [6], spinal stimulators [7], electric pain relievers [8], wireless sensors [9, 10, 11], micro-electromechanical systems [12, 13], etc., require minimal amounts of power to function. Such devices have, for a long time, relied on batteries that have not kept pace with the devices' demands, especially in terms of energy density [14]. In addition, batteries have a finite life span, adverse environmental impacts, and require regular replacement or recharging, which, in many of the previously mentioned examples, is a very cumbersome and expensive process.

Vibration-based energy harvesting is not envisioned as a replacement for large scale energy generation, but rather as a supplementary power source which will provide small amounts of energy for trickle-charge applications [15] or to power and maintain mobile devices and remote sensors installed in inaccessible locations, such as those in the human body, the hull of a ship, the support structure of a bridge, or the foundation of a building [9, 16]. It could also benefit developing healthcare technologies. Take, for example, bioengineering. The availability of a reliable, noninvasive power supply is a developmental constraint in that field. Sensors that can monitor everything from blood sugar to lactase concentrations are now being implanted in the human body. Spinal simulators, are also being utilized to send electrical signals that block chronic pain [7]. Ideally, these devices would be implanted with their power sources and function for the life of the patient. Supplemental surgeries to change power supplies are expensive and cumbersome and external power supplies wired to the device via skin-penetrating wires expose the patient to the risk of infection.

In light of these challenges, research is being conducted to implement vibration-based energy harvesters inside the human body. Some preliminary efforts indicated the possibility of harvesting up to 20 mW of power from the contraction of blood vessels caused by pulsating blood [17]. This energy can be used to power the telecommunication array on a DNA chip twice a day. Other areas of the body such as diaphragms, skeletal muscles, and shock transmitted through the joints are also being considered for energy harvesting [18].

Energy harvesting can also be very practical for powering sensors that monitor the health of structures [19]. One obstacle hindering this development has always been the availability of long-term, compact, and remote power sources. Batteries on average last no longer that 10 years, but structures often stand for several decades. In 2006, Elvin et al. [19] investigated the implementation of piezoelectric materials to harvest energy from vibrations caused by the flow of traffic over bridges, the swaying of a building, or even earthquakes. They concluded that powering such sensors with the harvested energy is not yet technologically feasible, but as the power consumption of modern electronics drops such technologies may become feasible.

Energy harvesting through various other techniques and for many other application has also been extensively studied. Piezoelectric "eels" were proposed to harvest energy from vortex shedding caused by the flow of a fluid around a blunt body [20]. Piezoelectric "windmills" were also designed and considered [21]. The feasibility of harvesting power from a backpack or shoe inserts was also discussed in the literature [22, 23]. Furthermore, concepts of energy harvesting from gun-fired munitions and similar applications that require high-G survivability were also introduced [24].

1.1.1 Vibratory Energy Harvesting Mechanisms

Energy from vibratory systems can be harvested using one of the following mechanisms:

1. **Electrostatic Energy Harvesting:** An electrostatic energy harvester scavenges power from the work done against an electric field. Mechanical energy can be converted into useful electrical energy by placing a charge on the plates of a variable capacitor and then moving them apart while constraining either charge or voltage [25]. One of the major advantages of electrostatic mechanisms is their scalability even to the microscale. They also do not require active materials and can generate voltages between two and ten volts. Disadvantages include the need to charge the capacitor to its maximum capacitance prior to being used for energy harvesting [25].

2. **Electromagnetic Energy Harvesting:** Electromagnetic harvesters rely on Faraday's law to generate power. A magnetic flux that changes with time produces current in a closed-loop conductor within the flux. Electromagnetic energy harvesters use the same method as electrical generators to produce power, but rely on external vibrations to move either the conductor or the magnet relative to one another. Electromagnetic energy harvesting has the advantages of not requiring smart materials or an external voltage source to scavenge power [26]. However, this method is not scalable and has low energy density because it requires both a magnet and a coil, which are bulky when compared to capacitive methods. Furthermore, output voltages of electromagnetic harvesters rarely exceed 0.1 Volts. Therefore, the voltage must be up-converted for practical applications, which usually results in significant losses.

3. **Magnetostrictive Energy Harvesting:** Magnetostriction can be defined as the ability of the material to deform when subjected to a magnetic field. While many ferromagnetic materials possess this feature, usually the strains obtained from magnetic interactions are very low and not suitable for practical applications. *Giant* magnetostrictive materials, on the other hand, undergo

considerable deformations when subjected to a magnetic field, and, hence, present themselves as a viable option to act as smart structures for sensing and actuation. Examples of such materials include Metaglass, Galfenol, and Terfenol-D with the latter being perhaps the most widely utilized [27, 28].

The significantly increased levels of magnetostriction make *Giant* magnetostrictive materials appealing for energy harvesting applications. Specifically, magnetostrictive materials can produce a time-varying magnetic flux when subjected to a time-varying strain. This magnetic flux can be used to generate current in a pick-up coil per Faraday's law. Advantages of magnetostrictive materials include *i)* high electromechanical coupling, *ii)* no depolarization issues, and *iii)* suitability for high frequency vibrations. Similar to an electromagnetic harvester however, magnetostrictive mechanisms require a pick-up coil and thus suffer from scalability limitations. Furthermore, magnetostrictive materials exhibit a non-linear behavior and require an external magnetic field, or bias, for optimal operations [26].

4. **Piezoelectric Energy Harvesting:** Piezoelectricity can be defined as the ability of the material to deform when subjected to an electric field and to develop and electric charge when deformed. The second property, also known as the inverse piezoelectric effect, forms the basis for energy harvesting using piezoelectric materials. These effects are most common in ceramics and crystals that have a tetragonal atomic lattice structure with a single ion at the center of the lattice [29]. Deforming or applying an electric field to the lattice causes the central ion to change quantum states. Piezoelectricity is present in natural minerals such as quartz, tourmaline, and bone as well as man-made ceramics such as lead zirconatetitanate (PZT) and lithium niobate. In recent years, a piezoelectric polymer known as polyvinylidene fluoride (PVDF) has also been developed, which is significantly more flexible than traditional piezoelectric materials and capable of increased power harvesting due to its ability

to tolerate greater strain. Advantages of piezoelectric energy harvesting include high electromechanical coupling, scalability, and the ability to operate in harsh environments. Some disadvantages include depolarization of the material under large strains, brittleness of piezoelectric crystals, and high output impedances.

1.1.2 Direct Excitation of a Piezoelectric Cantilever Beam for Energy Harvesting

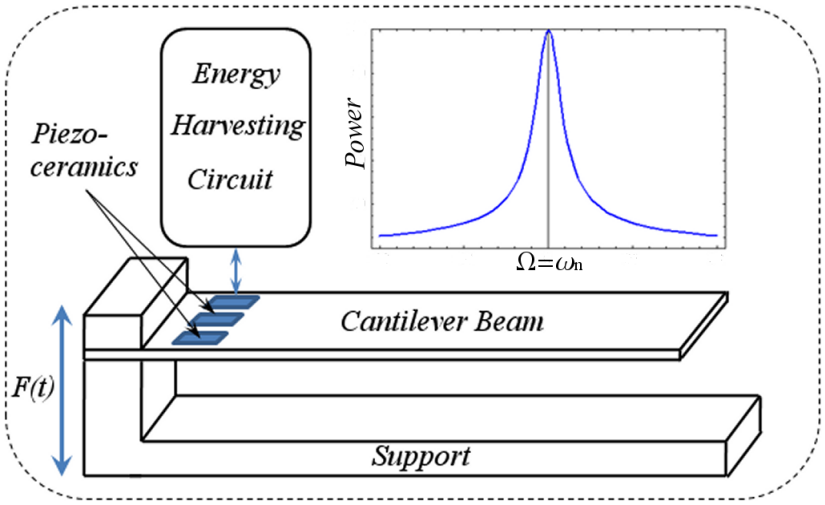

Figure 1.1: Schematic of a directly-excited cantilever-type harvester.

The principle behind vibrations-based energy harvesting is clearly illustrated by the most common energy harvester design: a cantilever beam subject to base excitations perpendicular to the beam's length as seen in Fig. 1.1. Attached to the surface of the beam near the clamped end are piezoelectric patches. If the base excitations are near one of the beam's infinite modal frequencies, the beam begins to oscillate which creates alternating strain near its clamped end. The piezoelectric patch converts the mechanical strain into an electric potential, or voltage, that alternates with the motion of the beam. Attaching an electric load to the piezoelectric patch creates a

complete AC circuit and allows power to be extracted from the environment.

Even with the plethora of energy harvesting approaches mentioned in Section 1.1.1 and the many others available in the literature [18, 1], cantilever-type energy harvesters remain the most prolific area of research. The most straight-forward approach uses either a uni- or bi-morph piezoelectric cantilever beam excited directly at its base. An extensive amount of literature has studied the optimization and active-tuning of these harvesters for maximum energy transfer. In one demonstration, DuToit et al. [30, 31, 32], among others [33, 34, 35, 36, 37], investigated the process of energy harvesting from *directly-excited* piezoelectric cantilever beams. They showed that, depending on the electric load, maximum energy flow from the environment occurs at the resonance and anti-resonance frequencies. Daqaq et al. [38] expanded upon that research by addressing the effect of mechanical damping on the optimal frequencies. They also demonstrated that, by adding an inductor to the harvesting circuit, maximum energy flow can be realized at any excitation frequency when an optimal inductance is implemented. Since maximum energy transfer from the environment to the electric load occurs when the excitation frequency is in the vicinity of one of the modal frequencies of the beam, many researchers have also investigated possible techniques to actively or passively tune the fundamental frequency of the harvester to the excitation frequency [39, 40, 35, 41, 42, 43, 44].

1.1.3 Parametric Excitation of a Piezoelectric Cantilever Beam for Energy Harvesting

While there is a tremendous amount of research detailing the modeling, optimization, and estimation of energy harvested through *directly-excited* cantilever beams (i.e. excited in a direction perpendicular to the beam's length), to our knowledge, no research has been conducted to study the process of energy harvesting using *parametrically-excited* beams (i.e. excited in a direction parallel to the beam's

length). Potential real-world energy harvesting applications often subject vibration-based energy harvesters to a myriad of multi-frequency excitations having various amplitudes and directions. Therefore, in addition to being directly-excited, a cantilever-type harvester may also be excited parametrically. As detailed in the next chapter, when a cantilever beam is subjected to parametric excitations at twice one of its infinite modal frequencies, a phenomenon known as the *principle parametric resonance* activates a dynamic instability causing finite-amplitude oscillations at half the excitation frequency [45, 46]. This thesis details an investigation of energy harvesting under such excitations.

1.2 The Parametric Instability

From a mathematical perspective, a dynamic system is said to be excited parametrically when the effect of forcing appears as a coefficient of a variable in the equations of motion. This arrangement causes a system to be non-autonomous, or time-varying, which usually complicates the response behavior and the associated dynamic analyses [47]. While, in general, it is well known that energy can be pumped into an oscillatory system at a frequency that is equal to or near its natural frequency inciting what is known as a *resonance condition*; the energy of an oscillating system may also be increased *by supplying energy at a frequency other than the fundamental frequency of the oscillator* [48]. A simple physical example is a child on a swing. To increase his amplitude of oscillation, the child lowers his center of gravity on the down swing and raises it on the up swing adding energy to the system at a frequency twice that of the swing [48]. Unknowingly, this child is activating a dynamic instability known as the *principle parametric resonance*. This phenomenon was first documented by Faraday in 1831 when he noted that a parametrically-excited column of fluid developed horizontal surface waves with a frequency equal to half that of the vertical excitation experienced by the fluid col-

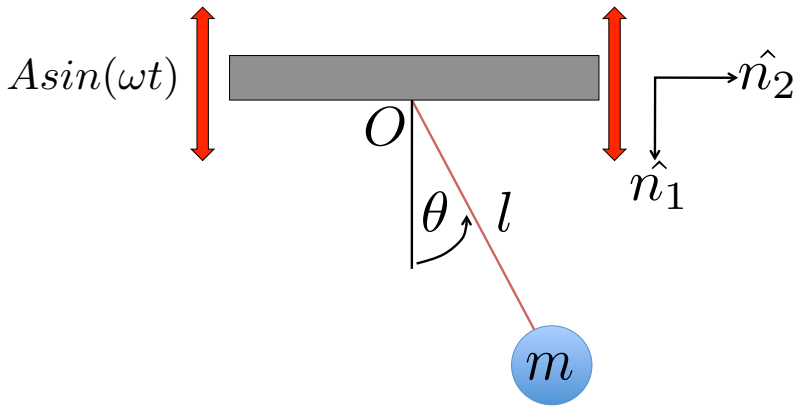

Figure 1.2: Schematic of a parametrically-excited pendulum.

umn [49]. A more readily observed experiment was carried out by Melde in 1859. He attached a string to a large tuning fork and excited the fork so that the direction of motion at the point of attachment was parallel to the length of the string. He then observed that the string oscillated at half the frequency of the tuning fork [50].

To better understand the parametric instability, its causes, and its influence on the response behavior of a dynamic system, we begin with a simple example: the parametrically-excited pendulum shown in Fig. 1.2. A pendulum of length, l, and mass, m, is subjected to a harmonic excitation of amplitude A and frequency ω in a direction parallel to its length when at rest. The excitation frequency is set near twice the natural frequency of the pendulum or, $\omega = 2\sqrt{\frac{g}{l}}$. Using an energy-method approach, we derive the equations of motion in terms of the oscillation angle, θ. The position vector to the pendulum mass, $\overline{OM}$, measured with respect to a stationary reference frame $(n - frame)$ is given by

$$\overline{OM} = (A\sin\omega t + l\cos\theta)\hat{n_1} + l\sin\theta\hat{n_2}. \tag{1.1}$$

Taking the derivative of the position vector with respect to time yields the velocity vector

$$^{N}v^{M/O} = (A\omega\cos\omega t - \dot{\theta}l\sin\theta)\hat{n_1} + \dot{\theta}l\cos\theta\hat{n_2}. \tag{1.2}$$

With that, the kinetic and potential energy of the system, T and V, respectively, can be written as

$$\begin{aligned} T = \frac{1}{2}m[(A\omega\cos\omega t - \dot{\theta}l\sin\theta)^2 + (\dot{\theta}l\cos\theta)^2], \\ V = -mgl\cos\theta, \end{aligned} \tag{1.3}$$

and the system's Lagrangian is

$$\mathcal{L} = T - V = \frac{1}{2}m[(A\omega\cos\omega t - \dot{\theta}l\sin\theta)^2 + (\dot{\theta}l\cos\theta)^2] + mgl\cos\theta. \tag{1.4}$$

Using the *Euler-Lagrange* Equation [51], the equations of motion of the pendulum can be written as:

$$\ddot{\theta} + \left(\frac{g}{l} + \frac{A}{l}\omega^2\sin\omega t\right)\sin\theta = 0 \tag{1.5}$$

Note the presence of the term $\frac{A}{l}\omega^2\sin(\omega t)\sin(\theta)$, which is the forcing term multiplied by the state variable, θ. This is what we refer to as a parametric excitation. Next, we use a Taylor series expansion of Equation (1.5) up to cubic terms in θ to obtain

$$\ddot{\theta} + \frac{c}{m}\dot{\theta} + \left(\frac{g}{l} + \frac{A}{l}\omega^2\sin\omega t\right)\left(\theta - \frac{\theta^3}{6}\right) = 0. \tag{1.6}$$

where $\frac{c}{m}\dot{\theta}$ is a viscous damping term added to account for mechanical damping effects.

To better understand the dynamics of Equation (1.6), we first non-dimensionalize the equation by introducing the non-dimensional time, $\tau \equiv t\omega_n$, where $\omega_n = \sqrt{\frac{g}{l}}$. This yields the following non-dimensional equation of motion:

$$\theta'' + \gamma\theta' + (1 + P\sin\Omega t)(\theta - \alpha\theta^3) = 0. \tag{1.7}$$

where

$$' = \frac{d}{d\tau},\ \gamma = \frac{c}{m\omega_n},\ \Omega = \frac{\omega}{\omega_n},\ P = \frac{A}{l}\Omega^2,\ \alpha = \frac{1}{6}. \tag{1.8}$$

Now, letting $\Omega \approx 2$ and scaling the system parameters as

$$\gamma = \epsilon\gamma,\ P = \epsilon P,\ \alpha = \epsilon\alpha, \tag{1.9}$$

where ϵ is a small bookkeeping parameter; we obtain using the Method of Multiple Scales [52]

$$\theta(t) = a_0 \sin\left(\frac{\Omega}{2}t - \frac{\gamma_0}{2}\right). \tag{1.10}$$

where a_0 is the steady-state amplitude of the pendulum response and γ_0 is the associated steady-state phase angle. It is worth noting that the frequency of the response is *half of the excitation frequency*. The steady-state amplitude, a_0 is obtained by solving

$$a_0^2\left[\gamma^2 + \left((\Omega - 2) + \frac{3}{4}\alpha a_o^2\right) - \frac{P^2}{4}\right] = 0. \tag{1.11}$$

Equation 1.11 reveals that the trivial solution, $a_0 = 0$, which results in no pendulum motion is always a solution. Solving for the non-trivial solutions $a_0 \neq 0$ yields

$$a_0 = \pm\sqrt{-\frac{4}{3\alpha}\left(\frac{(\Omega - 2)}{2} \pm \frac{1}{2}\sqrt{\frac{P^2}{4} - \gamma^2}\right)}. \tag{1.12}$$

As evident by Equation (1.12), for the non-trivial solutions to exist, i.e. to make the pendulum oscillate, the forcing term, P, must be greater than twice the damping, $P \geq 2\gamma$. If this condition is not satisfied, the parametric instability cannot be activated and no pendulum oscillations will occur. The principle parametric resonance curves are shown in Fig. 1.3 for different values of P and γ. The dashed lines represent unstable solutions (the stability of the solutions was assessed using the Jacobian of the modulation equations, which is not shown here). The region where the trivial solution is unstable coincides with the region where the non-trivial solutions are stable. This region represents the frequency bandwidth where the pendulum will undergo large-amplitude oscillations regardless of the initial conditions.

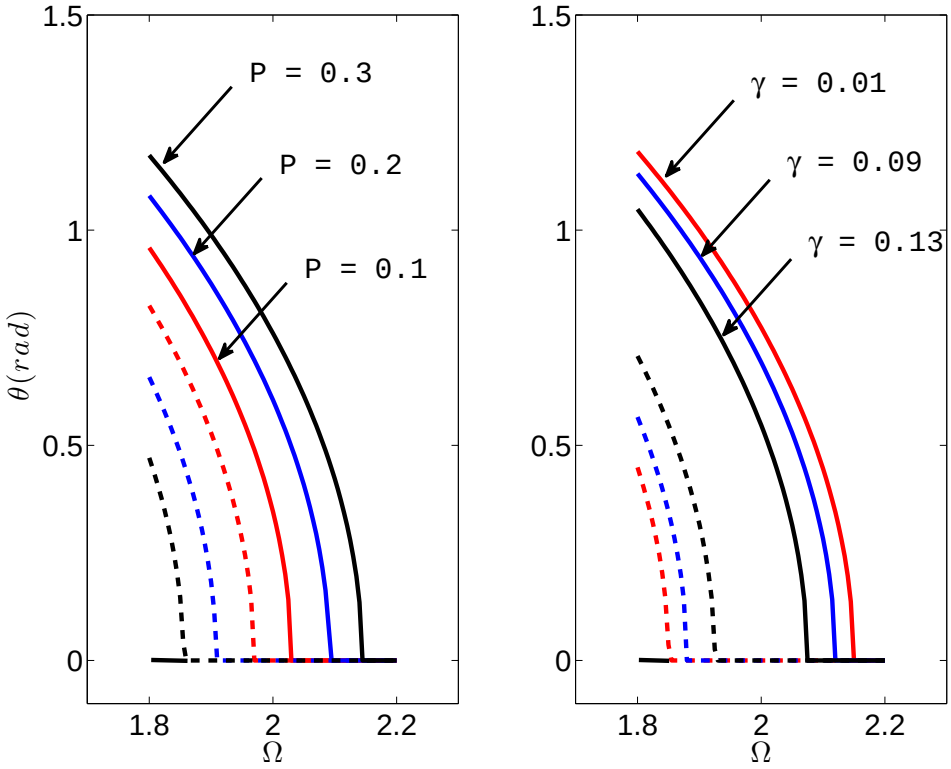

Figure 1.3: Steady-state principle-parametric resonance curves of the pendulum with different forcing and $\gamma = 0.4$ (right) and with different damping and $P = 0.3$ (left). The dashed lines represent unstable steady-state solutions.

Mathematically, this bandwidth is given by

$$-\sqrt{\frac{P^2}{4}-\gamma^2} \leq \Omega - 2 \leq \sqrt{\frac{P^2}{4}-\gamma^2}. \tag{1.13}$$

This implies that the bandwidth of the instability increases when γ decreases or P increases as can be further seen in Fig. 1.3. As such, to enlarge the bandwidth of response, we seek a source of excitation with large forcing and a structure with small damping. In fact, by minimizing the internal damping of the system, we also minimize the critical forcing required to activate the parametric instability and thus increase the number of potential excitation sources. This has important implications

when it comes to energy harvesting applications.

1.3 Thesis Contributions

This thesis marks the initial investigation of the behavior of parametrically-excited energy harvesters under harmonic (fixed-frequency), time-varying, and Gaussian random excitations. Specifically, the following items are addressed:

- The Method of Multiple Scales is utilized to obtain an approximate analytical expression for the steady-state output power of a parametrically-excited piezoelectric cantilever type harvester subjected to harmonic fixed-frequency excitations. The analytical results are validated against experimental data. The resulting expression is then utilized to understand the influence of the harvester's design parameters on the threshold excitation, the bandwidth of the harvester, and the output power.

- Most of the current efforts in energy harvesting research are focused on steady-state analyses and experimentations that employ a harmonic fixed-frequency base excitations [32, 53, 39, 54, 55, 56, 57, 58]. However, most environmental sources are non-stationary in nature having frequencies that drift with time, or can be considered as random, possessing energy on a wide bandwidth of frequencies. To fill this gap in the current knowledge, we will investigate the response of parametrically-excited energy harvesters under band-limited random excitations and excitations of time-varying frequency. Because of the complexity of obtaining analytical expressions for the response behavior in such scenarios. The work will be limited to a comprehensive experimental investigation.

- The thesis introduces the novel concept of the Softening-Hardening Hysteretic

Harvesters (SHHH) to enhance energy harvesting under time-varying frequency excitations.

1.4 Thesis Outline

The rest of the thesis is organized as follows: In Chapter 2, we use the Method of Multiple Scales to derive approximate analytical expressions for the steady-state amplitude and power output of a parametrically-excited cantilever-type harvester under harmonic, fixed-frequency excitations. We validate the results against experimental data, and use the resulting model to study the effect of the coupling coefficient and load resistance on the output power. We also investigate the critical forcing and bandwidth of the harvester under harmonic excitations.

In Chapter 3, we experimentally investigate the power output of a parametrically-excited cantilever-type harvester under time-varying frequency and band-limited random inputs. Two beams, one with a softening-type behavior and the other with a hardening-type behavior are studied. The effects of the sweep rate and sweep direction on the harvesting bandwidth and power output are analyzed. Based on the results of the analysis, a *Softening-Hardening Harvester* which is designed to maximize the power output from a time-varying frequency excitation source is introduced. Finally, each beam is studied under band-limited Gaussian random excitations to quantify the average power output of a parametrically-excited harvester in random environments. The effect of the bandwidth of excitations is also investigated.

In Chapter 4, we present specific conclusions regarding the behavior and potential uses of a parametrically-excited harvester along with recommendations for future work.

Chapter 2

Energy Harvesting Under Fixed-Frequency, Harmonic Excitations

2.1 Theoretical Analysis

To understand the process of energy harvesting using the parametric instability, we consider a parametrically-excited cantilever beam as shown in Fig. 2.1. For the purpose of energy harvesting, a piezoelectric patch is attached to the beam and connected to a resistive load. A lumped-parameter model representing the single-mode dynamics of the beam and the harvester can be written as [59]

$$\begin{aligned} &\ddot{u} + 2\mu_1^\star \dot{u} + \omega_n^2 u + \mu_2^\star |\dot{u}|\dot{u} + \alpha^\star u^3 + 2\beta^\star (u^2\ddot{u} + u\dot{u}^2) = u\frac{F^\star}{m}\cos(\omega t^\star) + \frac{\theta}{m}V^\star, \\ &\theta\dot{u} + C_p^\star \dot{V}^\star + \frac{1}{R}V^\star = 0, \end{aligned} \tag{2.1}$$

where u is a generalized co-ordinate representing the beam deflection in the x-direction, $V^\star$ is the output voltage measured across the resistor R, $\mu_1^\star$ is a viscous damping term, $\mu_2^\star$ is a quadratic damping term representing air drag, $\alpha^\star$ and $\beta^\star$ are

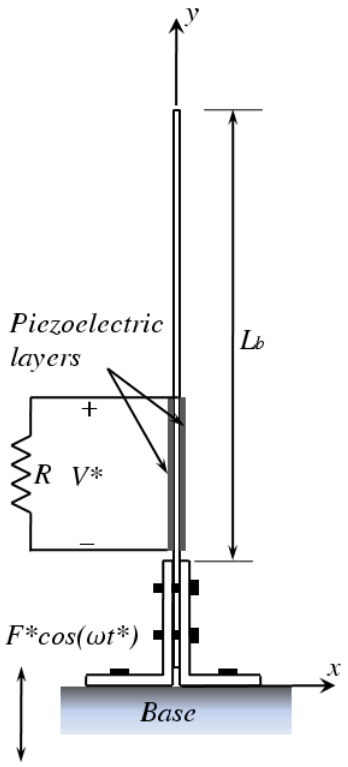

Figure 2.1: Schematic of a parametrically-excited cantilever-type harvester.

constants, θ is the electromechanical coupling term, $C_p^\star$ is the capacitance of the piezoelectric element, m is the effective mass of the beam, and $F^\star$ and ω are the excitation amplitude per unit length of the beam and the frequency, respectively. The term $\alpha^\star u^3$ is used to describe cubic geometric nonlinearities in the beam, and the term $2\beta^\star(u^2\ddot{u} + u\dot{u}^2)$ represents inertia nonlinearities. The beam deflection, u, and time, $t^\star$, can be further normalized with respect to the beam length, L_b, and the inverse of the response frequency $1/\omega_n$, respectively, to obtain

$$\begin{aligned} \ddot{x} + 2\mu_1\dot{x} + x + \mu_2|\dot{x}|\dot{x} + \alpha x^3 + 2\beta(x^2\ddot{x} + x\dot{x}^2) &= xF\cos(\Omega t) + \frac{\theta}{K}V \\ \theta\dot{x} + C_p\dot{V} + \frac{1}{R_{eq}}V &= 0 \end{aligned} \tag{2.2}$$

where

$$x = \frac{u}{L_b}, \qquad t = t^\star \omega_n, \qquad V = \frac{V^\star}{L_b}, \qquad \mu_1 = \frac{\mu_1^\star}{\omega_n}, \qquad \mu_2 = \mu_2^\star L_b, \qquad \alpha = \alpha^\star \frac{L_b^2}{\omega_n^2},$$
$$\beta = \beta^\star L_b^2, \qquad F = \frac{F^\star}{K}, \qquad C_p = C_p^\star, \qquad R_{eq} = R\omega_n, \qquad \Omega = \frac{\omega}{\omega_n}, \qquad K = m\omega_n^2. \tag{2.3}$$

To determine analytical expressions for the beam's deflection, output voltage, and power, we seek a uniform approximate analytical solution describing the behavior of the nonlinear system given by Equation (2.2) for small input excitations, damping, and nonlinearities. To that end, we utilize the Method of Multiple Scales and expand the deflection, x, and the voltage per unit length of the beam, V, as

$$x = x_0(T_0, T_1, T_2) + \epsilon x_1(T_0, T_1, T_2) + \epsilon^2 x_2(T_0, T_1, T_2) + O(\epsilon^3), \tag{2.4a}$$

$$V = V_0(T_0, T_1, T_2) + \epsilon V_1(T_0, T_1, T_2) + \epsilon^2 V_2(T_0, T_1, T_2) + O(\epsilon^3), \tag{2.4b}$$

where the $T_n = \epsilon^n t$ represent different time scales and ϵ is a small bookkeeping parameter that will be set to unity at the end of the analysis. In terms of the T_n, the time derivatives become

$$\frac{d}{dt} = D_0 + \epsilon D_1 + \epsilon^2 D_2, \qquad \frac{d^2}{dt^2} = D_0^2 + 2\epsilon D_0 D_1 + \epsilon^2 (D_1^2 + 2D_0 D_2), \tag{2.5}$$

where $D_n \equiv \partial / \partial T_n$. We order the coupling terms to appear at the second-order perturbation problem and order the forcing, F, so that it appears in the same perturbation equation as the damping and nonlinearities. As such, we let

$$\theta = \epsilon\theta, \qquad \mu_1 = \epsilon^2 \mu_1, \qquad F = \epsilon^2 F, \qquad \mu_2 = \epsilon^2 \mu_2, \qquad \alpha = \epsilon^2 \alpha, \qquad \beta = \epsilon^2 \beta. \tag{2.6}$$

Since the principle parametric resonance is activated near twice the modal frequency, finite beam oscillations necessary for energy harvesting can be activated when the beam is excited parametrically at twice its first modal frequency, i.e. $\omega = 2\omega_n$ or $\Omega \approx 2$ in nondimensional form. To that end, we introduce the detuning parameter,

σ, which characterizes nearness of the excitation frequency to twice the natural frequency, and let

$$\Omega = 2 + \epsilon^2 \sigma. \tag{2.7}$$

Substituting Equations (2.4a–2.7) into Equation (2.2) and equating coefficients of like powers of ϵ, we obtain

$$\begin{aligned} &O(1): \\ &\qquad D_0^2 x_0 + x_0 = 0, \end{aligned} \tag{2.8a}$$

$$C_p D_0 V_0 + \frac{1}{R_{eq}} V_0 = 0, \tag{2.8b}$$

$$\begin{aligned} &O(\epsilon): \\ &\qquad D_0^2 x_1 + x_1 = -2 D_0 D_1 x_0 + \frac{\theta}{K} V_0, \end{aligned} \tag{2.9a}$$

$$C_p D_0 V_1 + \frac{1}{R_{eq}} V_1 = -\theta D_0 x_0 - C_p D_1 V_0, \tag{2.9b}$$

$O(\epsilon^2)$:

$$\begin{aligned} D_0^2 x_2 + x_2 = &-2 D_0 D_1 x_1 - D_1^2 x_0 - 2 D_0 D_2 x_0 - 2\mu_1 D_0 x_0 - \alpha x_0^3 - 2\beta (x_0^2 D_0^2 x_0 \\ &+ x_0 (D_0 x_0)^2) + x_0 F \cos(2T_0 + \sigma T_2) - \mu_2 |D_0 x_0| D_0 x_0 + \frac{\theta}{K} V_1, \end{aligned} \tag{2.10a}$$

$$C_p D_0 V_2 + \frac{1}{R_{eq}} V_2 = -\theta D_1 x_0 - \theta D_0 x_1 - C_p D_2 V_0 - C_p D_1 V_1. \tag{2.10b}$$

The steady-state solution of the first-order problem, Equation (2.8), can be expressed as

$$\begin{aligned} x_0 &= A(T_1, T_2) e^{iT_0} + \bar{A}(T_1, T_2) e^{-iT_0}, \\ V_0 &= 0, \end{aligned} \tag{2.11}$$

where $A(T_1, T_2)$ is a complex-valued unknown function that will be determined by enforcing the solvability conditions at a later stage in the analysis and $\bar{A}(T_1, T_2)$ is

its complex conjugate. Substituting Equation (2.11) into Equation (2.9) yields

$$D_0^2 x_1 + x_1 = -2iD_1 A e^{iT_0} + cc, \tag{2.12a}$$

$$C_p D_0 V_1 + \frac{1}{R_{eq}} V_1 = -\theta i A e^{iT_0} + cc, \tag{2.12b}$$

where cc is the complex conjugate of the preceding term. The right-hand side of Equation (2.12a) contains a term of the form $e^{\pm iT_0}$ which potentially produces secular terms in the solution. Since we are seeking a uniform solution, we eliminate the secular terms from the right-hand side of Equation (2.12a) and obtain

$$D_1 A = 0 \Rightarrow A = A(T_2). \tag{2.13}$$

With this result, the solution of Equation (2.12b) can be written as

$$V_1 = -i \frac{\theta}{\frac{1}{R_{eq}} + iC_p} A e^{iT_0} + cc. \tag{2.14}$$

Substituting Equations (2.11) and (2.14) into Equation (2.10), then eliminating the secular terms from the outcome yields

$$i(2D_2 A + (2\mu_1 - \frac{\theta\lambda_i}{K})A) - \frac{\theta}{K}\lambda_r A + 8N_{eff} A^2 \bar{A} + \frac{\mu_2}{2\pi} \int_0^{2\pi} D_0 x_0 |D_0 x_0| e^{-iT_0} dT_0 - \frac{F}{2} \bar{A} e^{i\sigma T_2} = 0, \tag{2.15}$$

where

$$N_{eff} = \frac{3\alpha - 4\beta}{8}, \qquad \lambda_r = -\frac{C_p \theta R_{eq}^2}{1 + R_{eq}^2 C_p^2}, \qquad \lambda_i = -\frac{R_{eq}\theta}{1 + R_{eq}^2 C_p^2}.$$

In solving Equation (2.15), we find it convenient to express the complex function A in the polar form

$$A = \frac{1}{2} a(T_2) e^{i\eta(T_2)}. \tag{2.16}$$

Substituting Equation (2.16) into Equation (2.15), performing the integration, and separating the real and imaginary parts of the outcome yields

$$D_2 a = -\mu_{eff} a - \frac{4\mu_2}{3\pi} a^2 + \frac{F}{4} a \sin(\sigma T_2 - 2\eta), \tag{2.17a}$$

$$aD_2\eta = -\frac{\theta\lambda_r}{2K}a + N_{eff}a^3 - \frac{F}{4}a\cos(\sigma T_2 - 2\eta), \tag{2.17b}$$

where

$$\mu_{eff} = \mu_1 - \frac{\theta\lambda_i}{2K}. \tag{2.18}$$

The preceding nonautonomous system of equations, Equations (2.17), can be made autonomous by introducing the transformation

$$\gamma = \sigma T_2 - 2\eta, \tag{2.19}$$

and obtaining

$$D_2a = -\mu_{eff}a - \frac{4\mu_2}{3\pi}a^2 + \frac{F}{4}a\sin\gamma, \tag{2.20a}$$

$$aD_2\gamma = (\sigma + \frac{\theta}{K}\lambda_r)a - 2N_{eff}a^3 + \frac{F}{2}a\cos\gamma, \tag{2.20b}$$

Equations (2.20) are known as the modulation equations. The first of these equations, Equation (2.20a), is the amplitude equation because it describes how the amplitude of the response, a, evolves with time. The second equation, Equation (2.20b), is the phase or frequency equation because it describes how the phase, γ, of the response evolves with time. By solving these equations, it is possible to determine how the amplitude and frequency of the deflection, x, and output voltage, V, evolve with time.

Since Equations (2.20) play an imperative role in determining the characteristics of the harvester, we start by describing the important terms in these equations. The first term on the right-hand side of the amplitude equation, Equation (2.20a), represents the effective linear damping in the system. Note that this term consists of the structural damping, μ_1, and the electrical damping, λ_i. This term plays an important role in determining the response amplitude, a, and, hence the beam deflection, x, and output voltage, V. The second term on the right-hand side of Equation (2.20a) represents an effective quadratic damping term emanating from the air drag. This term also plays a critical role in limiting the growth of the response [45].

The first term on the right-hand side of Equation (2.20b) represents a measure of the difference between the natural frequency of the beam and the actual resonance frequency which is affected by the harvesting circuit through the term $\theta\lambda_r/K$. Finally, the coefficient $N_{eff}a^3$ represents a measure of the effective nonlinearity in the system. This term determines whether the response of the system is of the hardening or the softening type, which will be explained fully in Section 2.1.1.

2.1.1 Asymptotic Solutions and Their Stability

In the preceding discussion, we mentioned that the nonlinear response of the system can be obtained by solving Equations (2.20) for the amplitude, a, and phase, γ. Obviously, an analytical solution of these nonlinearly-coupled first-order ordinary differential equations is tedious, if not impossible. Luckily, when dealing with energy harvesting applications, one is certainly more interested in the steady-state responses, especially the steady-state voltage and power. To obtain the long-time behavior of the system, we set the time derivatives in Equations (2.20) equal to zero, then square and add Equations (2.20a) and (2.20b) to obtain

$$a_0\left[(\mu_{eff}+\frac{4\mu_2}{3\pi}a_0)^2+\left(N_{eff}a_0^2-\frac{1}{2}(\sigma+\frac{\theta}{K}\lambda_r)\right)^2=\frac{F^2}{16}\right]. \tag{2.21}$$

Equation (2.21) represents a nonlinear frequency-response equation that describes the implicit dependence of the steady-state response amplitude, a_0, on the detuning parameter, σ, and hence on the excitation frequency, Ω. Note that $a_0 = 0$ (*trivial solution*) is always a solution of Equation (2.21). The other solution (*nontrivial*) can be obtained by solving

$$(\mu_{eff}+\frac{4\mu_2}{3\pi}a_0)^2+\left(N_{eff}a_0^2-\frac{1}{2}(\sigma+\frac{\theta}{K}\lambda_r)\right)^2-\frac{F^2}{16}=0 \tag{2.22}$$

for a_0. The analytical solutions of Equation (2.22) were obtained using a commercial symbolic manipulator. However, since the resulting expressions for a_0 are long, we

elected not to list them in this manuscript. With the solution of Equation (2.22) available, we use Equation (2.4) to determine the normalized steady-state beam deflection, steady-state voltage drop per unit length of the beam, and the steady-state power dissipated in the resistor as

$$x_{ss}(t) = a_0 \cos\left(\frac{\Omega}{2}t - \frac{\gamma_0}{2}\right) + \mathcal{O}(\epsilon^3), \tag{2.23a}$$

$$V_{ss}(t) = \epsilon \frac{\theta}{\sqrt{\frac{1}{R_{eq}^2} + C_p^2}} a_0 \cos\left(\frac{\Omega}{2}t - \frac{\gamma_0}{2}\right) + \mathcal{O}(\epsilon^3), \tag{2.23b}$$

$$P_{ss} = \frac{|V^\star|^2}{R} = L_b^2 \frac{|V_{ss}|^2}{R} = \epsilon^2 L_b^2 \frac{\theta^2 R_{eq} \omega_n^2}{1 + R_{eq}^2 C_p^2} a_0^2, \tag{2.23c}$$

where

$$\gamma_0 = \arctan\left\{\frac{2\mu_{eff} + \frac{8\mu_2}{3\pi}a_0^2}{2N_{eff}a_0^2 - (\sigma + \frac{\theta}{K}\lambda)}\right\},$$

and $\epsilon = 1$. By examining Equations (2.23a) and (2.23b), it becomes evident that the response frequency is one half the excitation frequency. As such, exciting the beam parametrically at twice its first modal frequency causes the beam to vibrate at the first modal frequency, thereby producing an AC voltage having the beam's first modal frequency. The reader should also bear in mind that, the steady-state solutions, trivial or nontrivial, are not always stable and hence physically realizable. To assess the stability of the resulting steady-state solutions (a_0, γ_0), the eigenvalues of the Jacobian of the modulation equations, Equations (2.20), should be obtained. If all the resulting eigenvalues have negative real parts, the pair (a_0, γ_0) is locally asymptotically stable. Otherwise, if at least one eigenvalue has a positive real part, the pair (a_0, γ_0) is unstable and hence physically unrealizable.

To further clarify the concept of steady-state solutions, trivial and nontrivial, their stability and coexistence; we consider the case in which $\theta = 0$, i.e. the beam is completely decoupled from the electrical circuit. Using the solutions of Equation (2.22), which were obtained using the parameter values listed in Table 1, we plot variation of the steady-state amplitude with the excitation frequency in the vicinity of

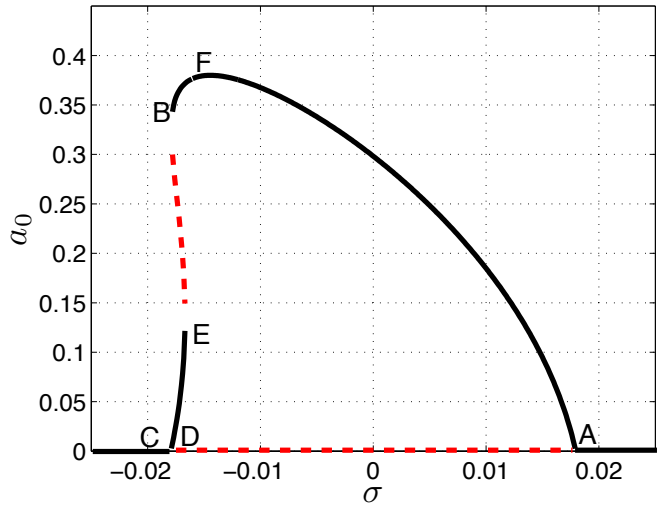

Figure 2.2: Frequency-response curves for $\theta = 0$ and $F = 0.05$. Dashed lines represent unstable steady-state solutions

the principle-parametric resonance (*frequency-response curve*), see Fig. 2.2. When $\theta = 0$, the beam exhibits large-amplitude responses and multivalued solutions for a range of the excitation frequencies. More specifically, as shown in Fig. 2.2, when $\sigma > \sigma_A$, only the stable trivial solution exists, $a_0 = 0$. As σ is decreased, the trivial solution loses stability at point A through a *supercritical-pitchfork* bifurcation giving way to a branch of stable periodic solutions causing the beam to oscillate periodically at half the excitation frequency. The amplitude of these oscillations increases as σ is decreased further towards point B. At point B, the periodic solution loses stability through a *saddle-node* bifurcation, and the response amplitude jumps down to point C (*jump phenomenon*) where only trivial solutions exist causing the beam oscillations to die out. Decreasing σ beyond point C leads only to the stable trivial solutions $a_0 = 0$.

Now, approaching from the right by increasing σ, only the trivial solution exists until we reach point C. Beyond this point, two stable solutions coexist. When the initial conditions are small, the system does not oscillate initially, and the response

Table 2.1: Parameters used in the numerical simulations.

Model Parameter	
Linear damping coefficient†, μ_1	0.00867
Nonlinear damping coefficient†, μ_2	0.01
Piezoelectric patch capacitance, $C_p[nF]$	570
Effective mass †, $m[g]$	43
Effective nonlinearity coefficient, N_{eff}	-0.05
Natural frequency†, $\omega_n[rad/sec]$	16.76

†These parameters were obtained experimentally for the beam shown in Fig. 2.9.

traces the trivial solution line CD. This solution loses stability through a transcritical bifurcation at point D giving way to stable nontrivial solutions that quickly encounter a saddle-node bifurcation at point E, leading to a jump to point F. Increasing σ further, the amplitude follows the curve FA where the trivial solutions are reached through a *supercritical pitchfork* bifurcation at point A. On the other hand, when the initial conditions are large, the response jumps to the nontrivial solutions at point B and follows the curves BA as σ is increased.

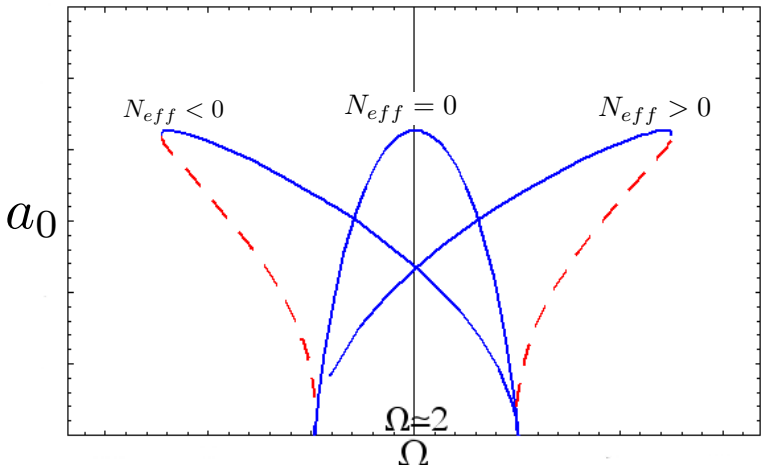

Figure 2.3: Effect of the effective nonlinearity (N_{eff}) on the shape of the steady state frequency response curve for a parametrically excited beam.

The effective nonlinearity $N_{eff} = \alpha - \frac{4}{3}\beta$, as obtained by the Method of Multiple Scales, determines whether the frequency-response curves bend to the left or to the right and the degree to which these curves bend. As shown in Fig. 2.3, when $N_{eff} = 0$, the frequency response curve is symmetric around $\Omega \approx 2$. In this case, the beam is linear and has poor broadband characteristics. The frequency response curve bends to the left (*nonlinear softening behavior*) when N_{eff} is less than zero and to the right when N_{eff} is greater than zero (*nonlinear hardening behavior*) [60]. The degree to which the curve bends depends on the magnitude of N_{eff}. The sign and magnitude of N_{eff} is determined by the magnitude of α and β which are both positive numbers. The coefficient α accounts for nonlinearities due to geometry or nonlinear curvature; β, on the other hand, accounts for nonlinear inertia. It has been shown that geometric nonlinearity produces a hardening effect, whereas inertial nonlinearity has a softening effect [46]. As such, depending on the strength of each term, the overall effect of the nonlinearities could be hardening or softening. For a beam, α and β are a function of the beam's geometry, material properties, boundary conditions, curvature, and mode shapes. By altering one or a combination of these parameters, the effective nonlinearity of the beam can be changed allowing the desired bend in the frequency response to be realized.

2.1.2 Electromechanical Coupling

We turn our attention to investigating the effect of electromechanical coupling, θ, on the amplitude of the steady-state deflection and output voltage. It should be realized that energy can *only* be harvested within the range of frequencies where the nontrivial solutions exist. Outside that range, only the trivial solution $a_0 = 0$ exists and no energy can be harvested per Equation (2.23c).

When the electromechanical coupling is increased from $\theta = 0\ N/Volts$ to $\theta = 0.00015\ N/Volts$, the steady-state beam deflection drops because some of the energy

is now being harvested and dissipated in the resistor R, as shown in Fig. 2.4. As a result, a steady-state voltage drop can now be measured across the resistor, as seen in Fig. 2.5. Further, because no unstable nontrivial solutions exist, the saddle-node bifurcation, which existed at $\theta = 0$ disappears, and the jump phenomenon ceases to exit.

When θ is increased to $\theta = 0.0002\ N/Volts$, the amplitude of the beam deflection drops further and the magnitude of the output voltage increases and shifts toward larger values of σ. This shift is due to an increase in the term $\theta\lambda_r/K$ which determines the actual resonance frequency as explained previously in the discussion following Equation (2.20b).

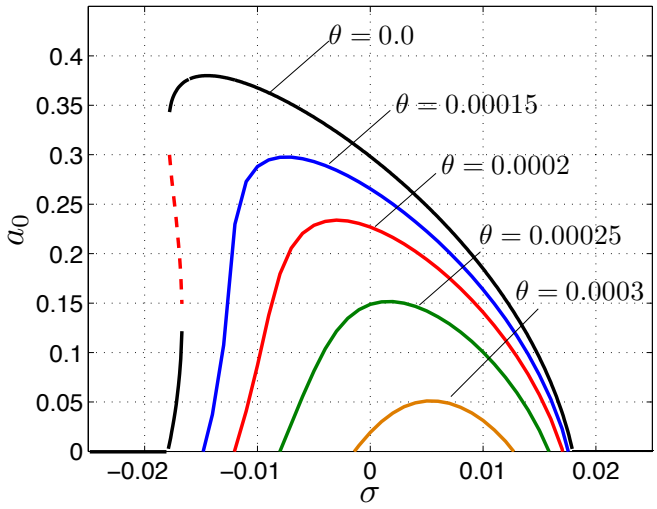

Figure 2.4: Voltage-response curves for different values of θ, $F = 0.05$, and $R = 90kOhm$.

Increasing θ towards $\theta = 0.00025\ N/Volts$ causes the response amplitude to drop even further, however, the output voltage does not increase as one would expect. This can be explained by examining Equation (2.23b) and noting that, for a given load resistance, the voltage is affected by two major parameters. These are the electromechanical coupling, θ, and the deflection amplitude, a_0. If a_0 remains constant as θ is increased, then one would surmise that increasing θ would cause the voltage

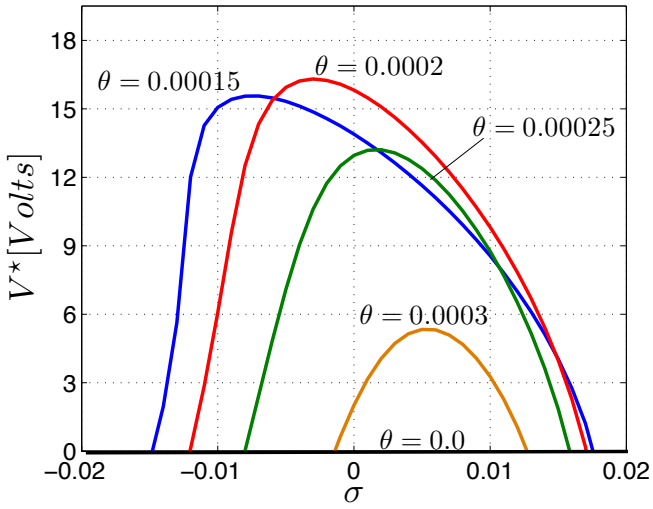

Figure 2.5: Frequency-response curves for different values of θ, $F = 0.05$, and $R = 90kOhm$.

output to increase. However, as clearly indicated in Fig. 2.4, as θ increases, a_0 does not remain constant and, in fact, decreases with θ. As such, there is an optimal response amplitude at which the energy harvested is maximized. This result agrees with the previous findings of Roundy et al. [61] and Daqaq et al. [38] who showed that, for a *directly-excited* beam, there is an optimal coupling coefficient beyond which the harvested power decreases. By maintaining an optimal load resistance the optimal power can even saturate as θ is increased.

It is also evident that the range of σ within which the nontrivial solutions exit, and hence power harvesting is possible, shrinks as θ increases. This is because, as θ increases, the effective damping, μ_{eff}, increases and larger excitations are required to initiate the parametric instability. If this force is not supplied by the environment, the range of frequencies wherein the instability occurs shrinks significantly causing a significant drop in the bandwidth of the harvester. For *directly-excited* beams, increasing θ causes the effective damping in the system to increase, thereby increasing the bandwidth of the response, and, hence having an opposite effect on the broad-band characteristics of the harvester.

The two curves shown in Fig. 2.6 represent the critical values of the frequency-detuning parameter σ as a function of the coupling coefficient θ. For a given coupling coefficient, values of σ (excitation frequency) falling in between these curves yield nontrivial solutions, and hence, output power. On the other hand, any value of σ falling outside these curves yields only the trivial solution and hence no power can be harvested. As θ is increased, both of these curves come closer together until they collide at $\theta_{cr} \approx 0.00033\ N/Volts$. Beyond this value of the coupling coefficient, no power can be harvested because the nontrivial solutions cannot be excited for a given forcing, F. Increasing the forcing would essentially extend these curves to larger values of θ.

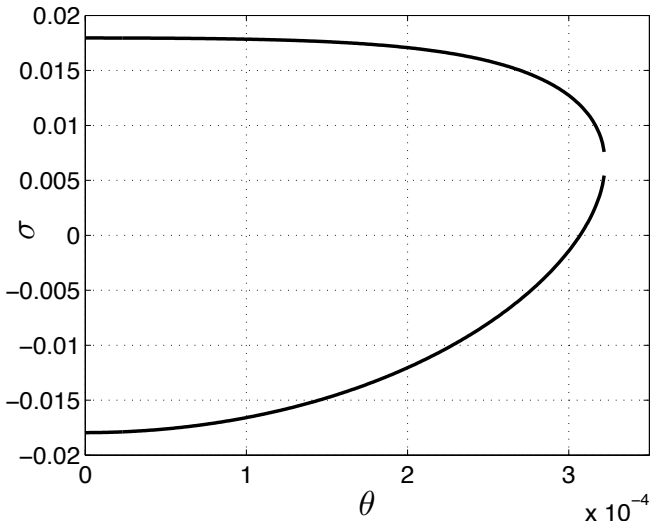

Figure 2.6: Variation of the critical values of σ with the coupling coefficient θ. Results are obtained for $R = 90\ kOhm$ and $F = 0.05$.

2.1.3 The Critical Excitation

When a beam is directly excited near one of its modal frequencies, energy is transferred from the environment to the beam causing the beam to oscillate even when the excitation amplitude is very small. Unfortunately, this is not the case for a

parametrically-excited beam. Equation (2.21) possesses nontrivial solutions only when the forcing, F, exceeds a critical value F_{cr}. Otherwise, the only existing solution is $a_0 = 0$ and the beam does not undergo any finite-amplitude oscillations. As such, for energy harvesting to be possible, a minimum value of the excitation amplitude should be maintained. To further explain this concept, we consider the case when $\mu_2 = 0$ and solve Equation (2.21) for the nontrivial solutions to obtain

$$a_0 = \pm\sqrt{\frac{1}{N_{eff}}\left\{\frac{(\sigma + \frac{\theta}{K}\lambda_r)}{2} \pm \sqrt{\frac{F^2}{16} - \mu_{eff}^2}\right\}} \tag{2.24}$$

By examining Equation (2.24), it becomes evident that, when $F < 4\mu_{eff}$, the nontrivial solutions cease to exist, and no power can be harvested per Equation (2.23c). The magnitude of the critical forcing is determined by the effective damping in the system, μ_{eff}, which, in turn, depends on the viscous damping, μ_1, the electromechanical coupling, θ, the load resistance, R, and the piezoelectric capacitance, C_p. Figure 2.7 depicts variation of F_{cr} with the load resistance, R, for different values of the coupling coefficient θ. The higher the coupling coefficient, the larger the forcing required to excite the beam parametrically. Furthermore, as the resistance is increased for a given coupling coefficient, the critical forcing increases for small values of R and peaks at a given load resistance. The resistance at which the peak occurs can be easily obtained by differentiating μ_{eff} with respect to R_{eq} and solving the resulting equation for R. This yields

$$R_{peak} = \frac{1}{C_p\omega_n} \tag{2.25}$$

Beyond this peak value, the critical forcing decreases and becomes constant for very large resistances.

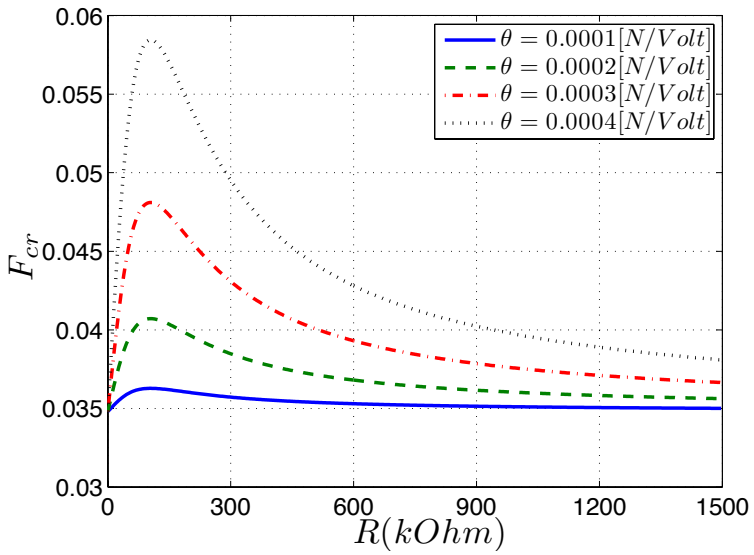

Figure 2.7: Variation of F_{cr} with the load resistance, R, for different coupling coefficients, θ.

2.2 Experiments:

2.2.1 Setup

The experimental setup shown in Fig. 2.9 was designed to validate the results by capturing three parameters: lateral beam deflection, output voltage across the resistor, and the dissipated power. The mechanical part of the harvester consisted of a 85 mm $\times$ 28 mm Macro Fiber Composite (MFC) patch attached to a stainless steel beam. The beam has an effective length of 304.8 mm, a width of 31.75 mm, and a thickness of 0.51 mm as well as a 30.1 g tip mass. The beam is clamped on a 50 mm deep aluminum fixture which is mounted on a LabWorks Inc. ET-139 electrodynamic shaker. A summary of the physical and electrical properties of the MFC and beam can be found in Table 2.

The shaker is used to excite the beam parametrically near twice its first modal frequency with a constant forcing equal to 0.32 g. The resulting lateral deflection is measured using a laser displacement sensor and the output voltage is recorded using

Table 2.2: Geometric and material properties.

Beam	
Modulus of elasticity, $[GPa]$	193
Density, $[kg/m^3]$	8027
Length, $L_b[mm]$	304.8
Width, $[mm]$	31.75
Thickness,$[mm]$	0.51
Tip mass, $[grams]$	30.1
MFC patch	
Length, $[mm]$	85
Width, $[mm]$	28
Thickness, $[mm]$	0.3
Capacitance, $C_p[nF]$	570
Coupling coefficient, $\theta[N/Volts]$	0.00022

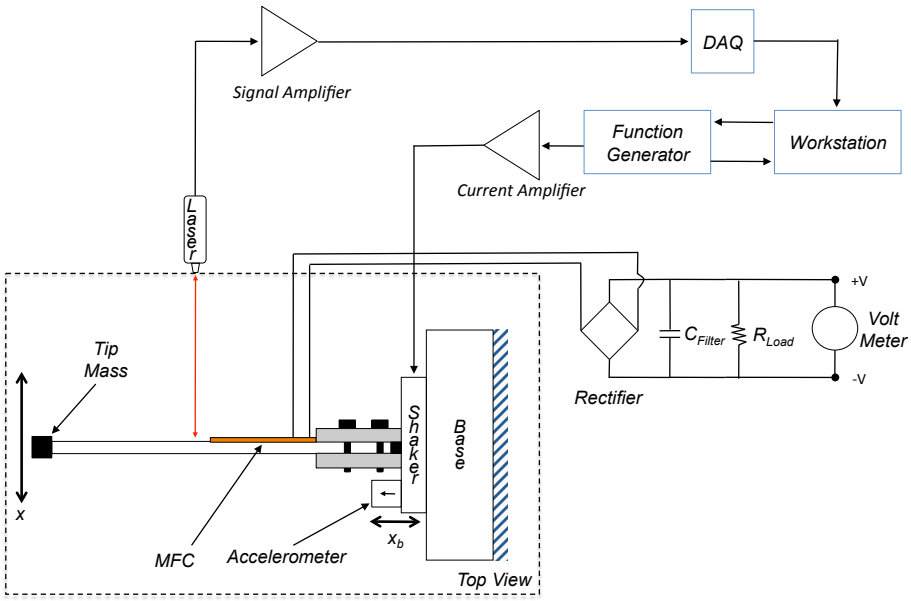

Figure 2.8: Schematic of the experimental setup for the fixed-frequency, harmonic excitations

a Fluke 112 true RMS digital multi-meter. A schematic of the experimental setup and the experimental setup itself are shown in Fig. 2.8 and Fig. 2.9, respectively.

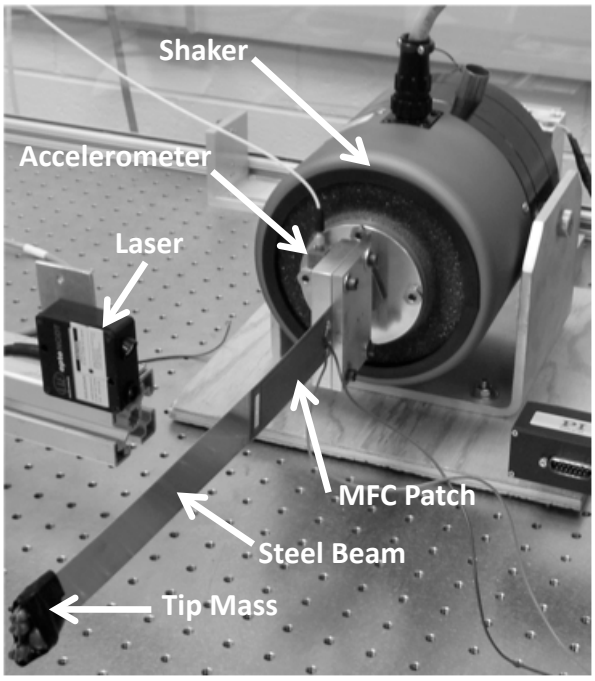

Figure 2.9: Experimental setup for the fixed-frequency, harmonic excitations

2.2.2 Influence of the Load Resistance

We begin by studying the effect of the load resistance on the output voltage as shown in Fig. 2.10. Although the match between the theoretical and experimental results is not perfect, the predictions demonstrate very good agreement and show the right trends which validates the theoretical modeling and analysis framework adopted in this manuscript. The reason for the slight mismatch between the experimental and theoretical findings is attributed to air drag which varies from one set of experiments to the other and is not easy to quantify. Anderson et al. [45] demonstrated that the amplitude of the beam deflection near the parametric instability is very sensitive to air damping, and hence, can change the amplitude considerably.

By inspecting Fig. 2.10, we note that, as the load resistance increases, the output voltage increases and the peak frequency shifts towards larger values of the excitation frequency. Further investigation reveals that the peak frequency shifts from twice

the resonance frequency, $\omega_r = 2.66\ Hz$, to twice the anti-resonance frequency, $\omega_{ar} = 2.68\ Hz$, which were measured experimentally at short- and open-circuit conditions, respectively. Since, as mentioned in Section 2.1, the term $\lambda_r\theta/K$ determines the actual resonance frequency of the system; we use this term to study variation of the resonance frequency with the load resistance R as depicted in Figure 2.11. Again, it can be clearly seen that the peak frequency varies from $2\omega_r$ when $R \rightharpoonup 0$ to $2\omega_{ar}$ when $R \rightharpoonup \infty$.

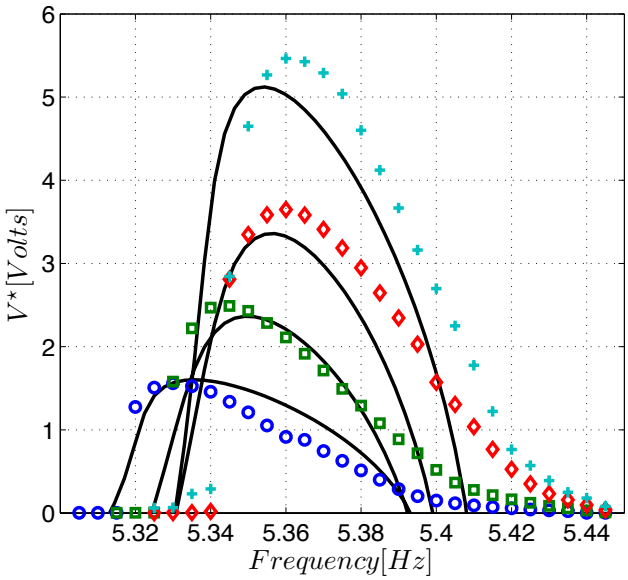

Figure 2.10: Experimental and theoretical frequency-response curves for different values of R, and $\theta = 0.00022N/Volts$. $R = 100\ kOhm$ (circles), $R = 250\ kOhm$ (squares), $R = 500\ kOhm$ (diamonds), $R = 1000\ kOhm$ (crosses).

It can also be noted that the range of frequencies wherein the nontrivial solutions exist shrinks and expands depending on the resistance value. This, in turn, affects the bandwidth of the harvester. To obtain the range of the frequencies wherein the parametric resonance can be activated for a given load resistance, we set $a_0 = 0$ in Equation (2.21) and solve the resulting equation for σ to obtain

$$\sigma_{cr} = -\frac{\theta\lambda_r}{K} \pm \frac{1}{2}\sqrt{F^2 - 16\mu_{eff}^2} \tag{2.26}$$

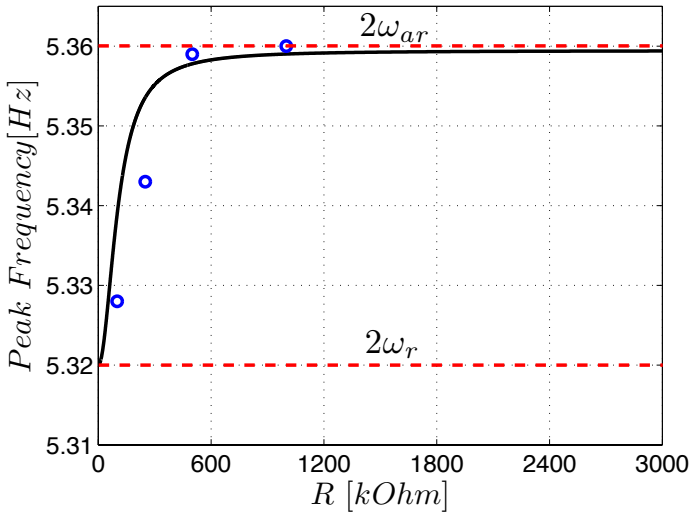

Figure 2.11: Variation of the peak frequency with the load resistance for $\theta = 0.00022\frac{N}{Volts}$. Circles represent experimental results.

The preceding expression defines the range of frequencies within which energy can be harvested. It is worth mentioning that this range is determined by the linear parameters and does not depend on the nonlinear damping, μ_2, or the effective nonlinearity coefficient, N_{eff}, which only play a role in determining the amplitude of the output voltage. Using Equation (2.26), we plot variation of σ_{cr} with the load resistance, as shown in Fig. 2.12. Any excitation frequency outside these curves yields no output power.

Variation of the output power with the excitation frequency is depicted in Fig. 2.13. There is a larger deviation between the theoretical and experimental results when compared to the voltage measurements shown in Fig. 2.10. The reason stems from the fact that the output power is obtained by squaring the voltage drop across the resistor and dividing the outcome by the resistor value. As such, the error in the power calculation is expected to be larger. It can also be noted that, while the voltage drop increases with the load resistance, the output power does not. To further emphasize this finding, we plot variation of the output voltage and power

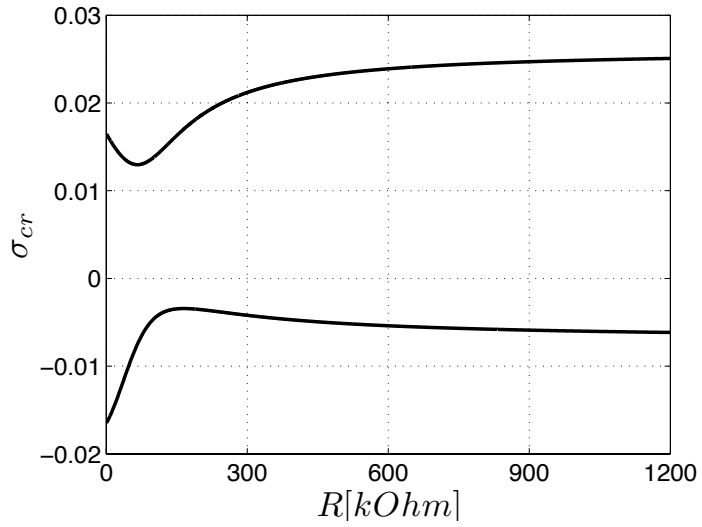

Figure 2.12: Variation of σ_{cr} with the load resistance. Results are obtained for $\theta = 0.00022 \frac{N}{Volts}$.

with the load resistance for an excitation frequency $\Omega = 5.37\ Hz$. By examining Figs. 2.14 and 2.15, it can be clearly seen that, while the output voltage continues to increase and plateaus as $R \rightharpoonup \infty$, the output power increases initially, reaches a maximum at an optimal load resistance, then decreases again as the load resistance is increased beyond the optimal value. This is the same trend that power harvested from a directly-excited beam follows.

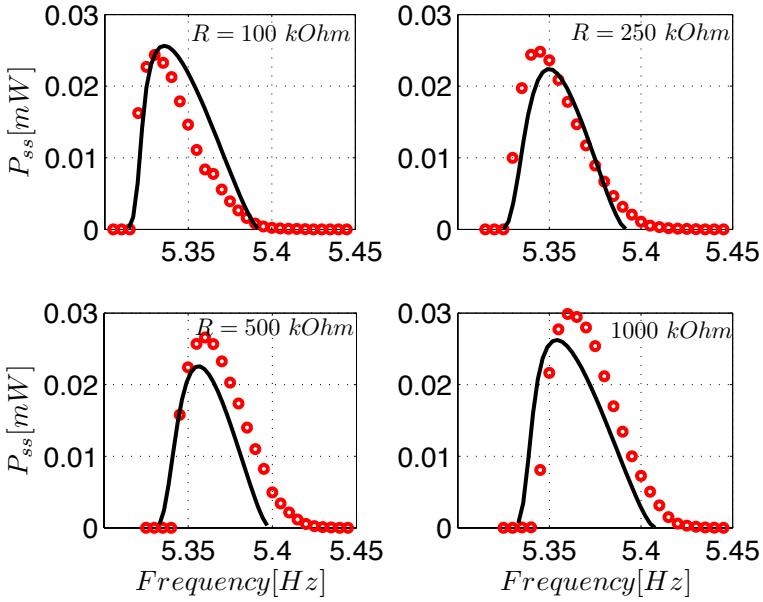

Figure 2.13: Experimental and theoretical power-frequency curves for different values of the load resistance R and $\theta = 0.00022 \frac{N}{Volts}$. Circles represent experimental results.

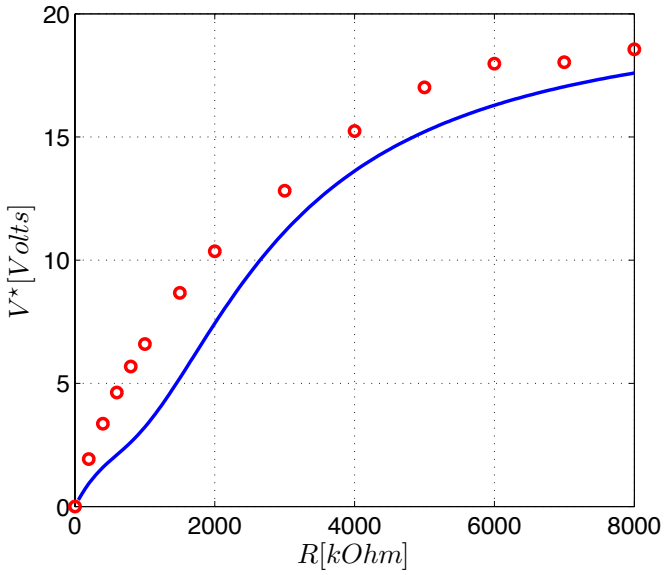

Figure 2.14: Variation of the output voltage with load resistance R. Results are obtained for $\theta = 0.00022$ and excitation frequency equal to 5.37 Hz. Circles represent experimental results.

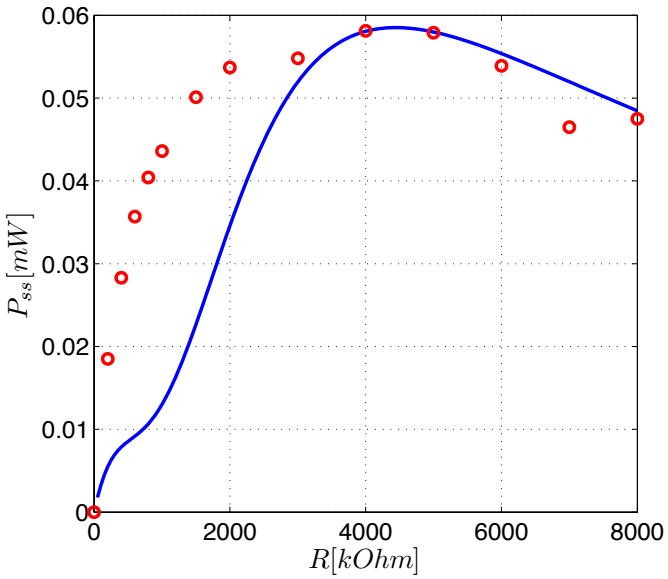

Figure 2.15: Variation of the output voltage with load resistance R. Results are obtained for $\theta = 0.00022$ and excitation frequency equal to 5.37 Hz. Circles represent experimental results.

Chapter 3

Energy Harvesting Under Time-Varying Frequency & Gaussian Random Excitations

3.1 Motivations

Much of the current research on energy harvesting has dealt with power generation from a stationary excitation source (*usually harmonic with a fixed frequency*). However, environmental excitations to which harvesters are generally exposed are non-stationary or random in nature. It is difficult to imagine a realistic application where that harvester is excited at a single fixed frequency outside of the laboratory. In addition, it is still not well-understood whether a harvester's performance under steady-state conditions is a good indicator of its performance in a realistic environment.

This chapter deals with understanding the transduction of a parametrically-excited harvester under time-varying frequency and random excitations. Since obtaining a

closed-form analytical solution in such cases is a formidable task, we limit our study to a detailed experimental investigation.

3.2 Experimental Setup

Table 3.1: Parameter values for the hardening and softening beams

Parameter	**Softening Beam**	**Hardening Beam**
Beam Dimensions	$133.0 \times 14.6 \times 0.5\ mm$	$133.0 \times 14.6 \times 0.5\ mm$
Beam Material	Low Carbon Steel	Low Carbon Steel
Beam Density	$7850\ \frac{kg}{m^3}$	$7850\ \frac{kg}{m^3}$
Beam Young's Modulus	$210\ GPa$	$210\ GPa$
Mechanical Damping Ratio	0.00834	0.00799
Adhesive	Ethyl Cyanoacrylate	Ethyl Cyanoacrylate
Tip Mass	$45\ g$	$36\ g$
Parametric Resonance	$8.6\ Hz$	$8.875\ Hz$
MFC Dimensions	$85.0 \times 7.0 \times 0.3\ mm$	$85.0 \times 7.0 \times 0.3\ mm$
MFC Young's modulus	$30\ GPa$	$30\ GPa$
Piezoelectric Constant	$-170\ \frac{pC}{N}$	$-170\ \frac{pC}{N}$

Two harvesting beams are constructed of identical materials, see Table 3.1, and are tuned to approximately the same principle parametric frequency. Though both harvesters were cut from the same stock, it was observed that one harvester exhibits a *hardening* behavior ($N_{eff} > 0$) under parametric excitation, and is, henceforth, known as the *hardening beam*, while the other harvester exhibits a *softening* behavior ($N_{eff} < 0$) and is, henceforth, known as the *softening beam*. Both beams were observed to have a mild torsional deformation, but the softening beam is also lightly curved. Previous studies have shown that a curved beam can exhibit a softening frequency response [62].

The steady-state, principle parametric curves shown in Fig. 3.1 for both beams exhibit their respective non-linearities. The softening beam is observed to exhibit smaller amplitude for the same input accelerations. We attribute this behavior to

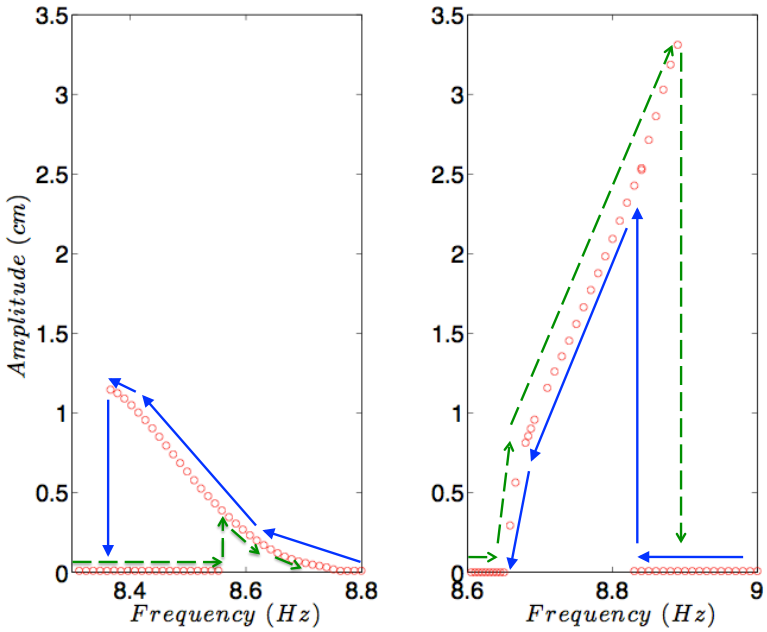

Figure 3.1: Principle parametric response curves of the softening beam (left) and the hardening beam (right). Solid arrows denote a reverse sweep and dashed arrows denote a forward sweep.

the thicker adhesive layer that bonds the piezoelectric patch to the steel beam. This resulted in an overall stiffer response with a higher damping ratio. Because of the increased stiffness, an extra 9 g tip mass was added to the softening beam to produce a fundamental frequency comparable to the hardening beam.

Both beams were excited using a LabWorks E-139 Electrodynamic Shaker. The amplitude was measured at a point 66 mm from the base of the beam with a laser vibrometer. The piezoelectric patch, a Macro-Fiber Composite (MFC) from Smart Material Corporation, was connected to a purely resistive load. The experimental set-up is depicted in Fig. 3.2.

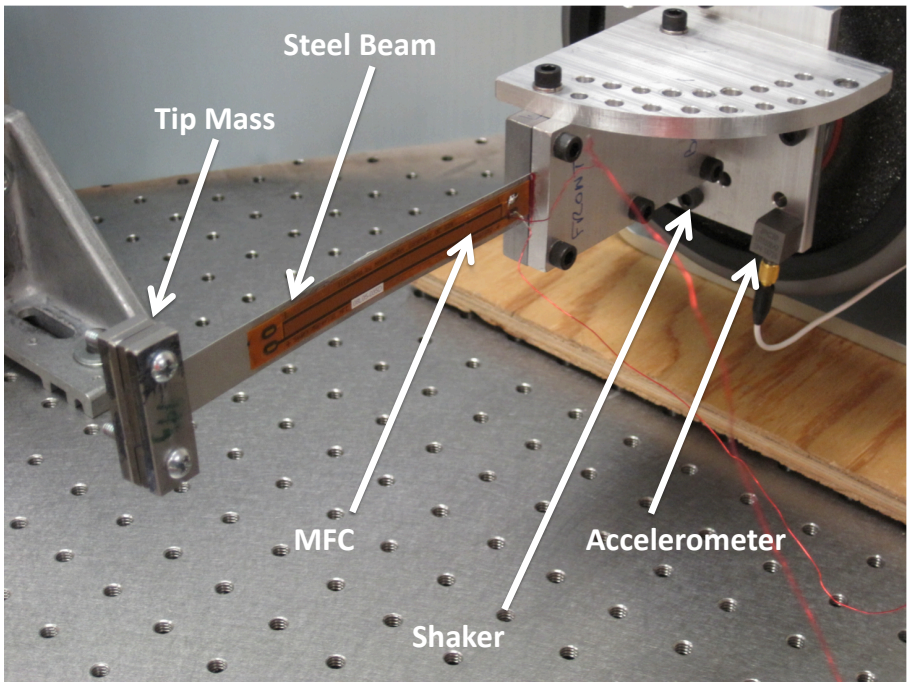

Figure 3.2: Experimental set-up utilized for time-varying frequency and random excitations study.

3.3 Harvesting under Time-Varying Frequency Excitations

Both beams were subjected to linear, time-varying frequency excitations having the form $\Omega(t) = \Omega_0 \pm st$. Here Ω_0 is the starting frequency and s is the sweep rate. The sign of s changes depending on the direction of the frequency sweep. A *forward* sweep, where $\Omega_0 < \Omega_f$ (Ω_f denotes the terminal frequency), is $\Omega_0 + st$, and a *reverse* sweep, where $\Omega_0 > \Omega_f$, is $\Omega_0 - st$. For each sweep, the input acceleration remained constant at 0.8 g and Ω_0 and Ω_f were chosen at about 0.1 Hz outside the steady-state response bandwidth for each beam.

3.3.1 The Hardening Beam

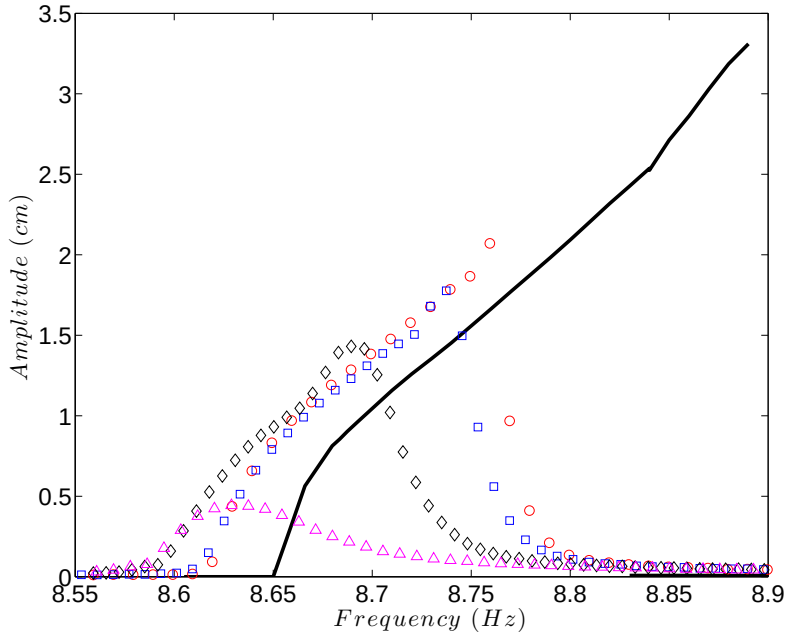

Figure 3.3: Variation of the response amplitude with the excitation frequency under various reverse sweep rates for the hardening beam. Steady state (solid line), $s = 1\ \frac{mHz}{s}$ (circles), $s = 2\ \frac{mHz}{s}$ (squares), $s = 3.27\ \frac{mHz}{s}$ (diamonds), and $s = 4.25\ \frac{mHz}{s}$ (triangles).

Figure 3.1 illustrates that the bandwidth of the hardening beam is 0.24 Hz at steady state. When subjected to a *reverse* frequency sweep, the bandwidth decreases as the sweep rate increases until the parametric response becomes unexcitable just above $s = 4.25\ \frac{mHz}{s}$ as shown in Fig. 3.3. For very low sweep rates, the response follows the steady-state response curve in the reverse direction. Specifically, when the frequency of excitation is decreased, the response of the harvester follows the stable trivial (zero oscillation) branch of solution up to the high end of the instability region where it suddenly jumps to the stable non-trivial branch of solutions and continues to follow that branch until it exits the parametric instability. As the sweep rate is increased, the beam has less time to respond to the instability because of the response time

constant. This causes the bandwidth of the response to decrease and the frequency response peak to shift toward lower frequencies. For instance, a sweep rate of just 1 $\frac{mHz}{s}$ results in a 17% decrease in bandwidth from the steady-state response while a sweep rate of 4.25 $\frac{mHz}{s}$ results in a bandwidth reduction of 28%. Also, it is observed that the peak response amplitude, and by extension the power output, decreases and shifts toward lower frequencies as s increases.

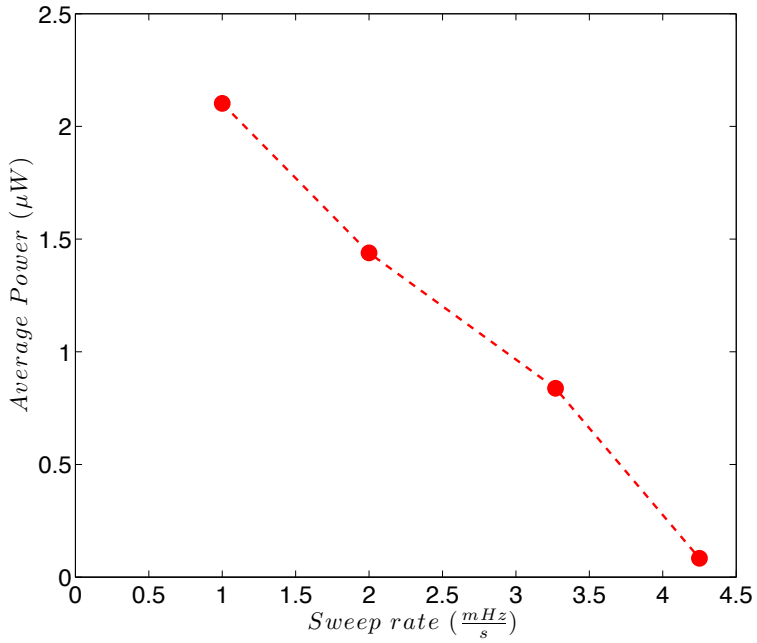

Figure 3.4: Variation of the average power output with the sweep rate for a reverse sweep spanning the range between 9.0 Hz and 8.6 Hz. Results are obtained for the hardening beam.

Figure 3.4 demonstrates that, as the sweep rate increases, the average power per sweep cycle for the hardening beam decreases. There is also a maximum sweep rate, beyond which no power can be harvested. The highest average power output per cycle for the hardening beam under a reverse sweep is 2.1 μW at $s = 1 \frac{mHz}{s}$. This relatively low power output is partially the result of the non-optimal resistive load used during the experiments. Figure 3.5 shows the optimal resistance curve for

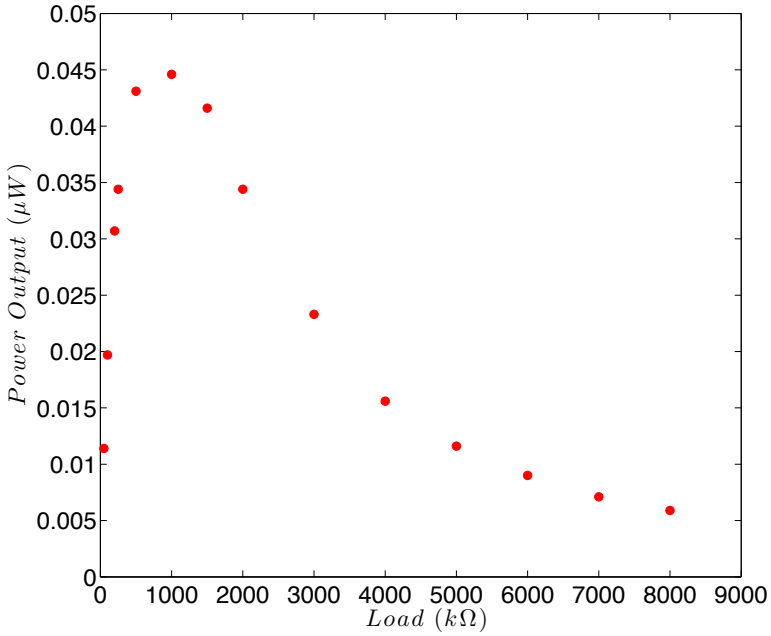

Figure 3.5: Variation of the output power with the load resistance at 8.6 Hz for the softening beam. The curve is identical for the hardening beam.

both beams. The optimal resistance is a function of the internal resistance of the piezoelectric patch, its capacitance, and the frequency of oscillations. Since both beams were constructed using the same MFC patch and have similar resonance frequencies, they were found to exhibit an equivalent optimal resistance of about $1M\Omega$. Though the optimal resistance is $1M\Omega$, all experiments were conducted with a load of $8M\Omega$. According to Fig. 3.5, using the $8M\Omega$ resistance results in 87% less output power than what could have been achieved if the load is optimized.

Figure 3.6 depicts the response of the hardening beam to a *forward*, linear, frequency sweep. The sweep in this instance is toward large frequencies, the direction in which the steady-state curve bends. First, we note that, for very small sweep rates, e.g. $s = 2\ \frac{mHz}{s}$, the time-varying frequency response curves are very similar to the steady-state curve. In other words, the sweep rate is on a much slower time scale than the beam dynamics, such that it does not interact with the beam response;

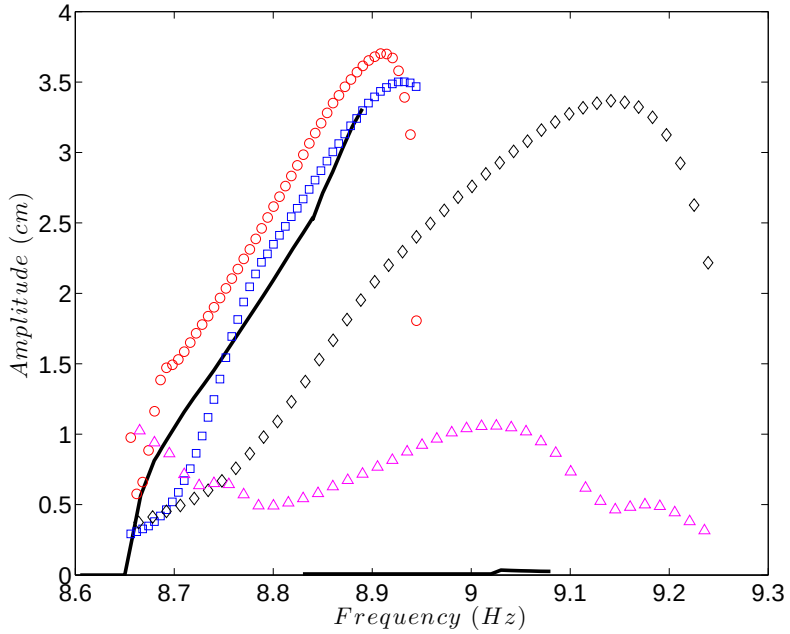

Figure 3.6: Variation of the response amplitude with the frequency under various forward sweep rates for the hardening beam. Steady state (solid line), $s = 2\ \frac{mHz}{s}$ (circles), $s = 6\ \frac{mHz}{s}$ (squares), $s = 14\ \frac{mHz}{s}$ (diamonds), $s = 30\ \frac{mHz}{s}$ (triangles).

the result is that the time-varying frequency response is almost identical to the steady-state response. As the sweep rate increases, e.g. $s = 14\ \frac{mHz}{s}$, the peak in the frequency-response curves decreases and shifts to toward higher frequencies due to system inertia. This has the effect of extending the bandwidth of the harvester to about 0.63 Hz which is more than twice that of the steady-state response. For very fast sweep rates, e.g. $s = 30\ \frac{mHz}{s}$, the beam still responds to the parametric instability but the peak response becomes very small and shifts toward even higher frequencies.

The average power output per sweep cycle decreases with increasing sweep rate as one would expect given the behavior of the response curves. The one exception is the power output for $s = 14\ \frac{mHz}{s}$ which is greater than for the slower sweep rates

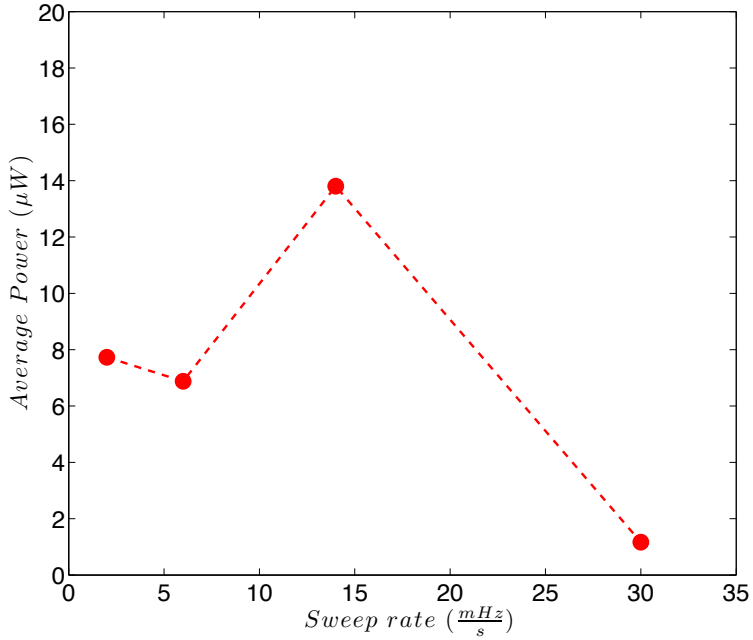

Figure 3.7: Variation of the average power output with the sweep rate for a forward sweep spanning the range between 8.60 Hz and 9.24 Hz. Results are obtained for the hardening beam.

because the system inertia greatly expanded the bandwidth over which power was harvested.

Compared to the *reverse* sweep, the *forward* sweep generates a higher average power. Because in the forward direction, the sweep moves in the direction in which the steady-state response curve bends, the parametric instability is excitable over a larger bandwidth, which leads to power being harvested for a longer period of time. Also, as the instability is activated, the inertia of the system allows the bandwidth to extend outside the steady-state bandwidth which also increases the average power per cycle. Furthermore, as the frequency increases, the response follows the stable non-trivial solution in the forward direction. The maximum amplitude of the response in this direction will always be greater than the amplitude of the response in

the opposite direction. This implies that more power will always be generated when the sweep is in the same direction of the bending of the frequency-response curves.

3.3.2 The Softening Beam

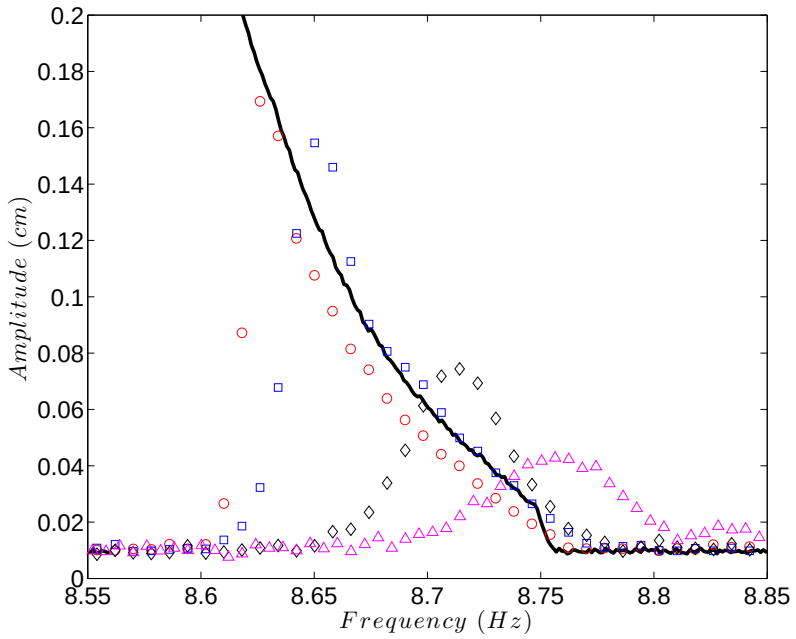

Figure 3.8: Variation of the response amplitude with the excitation frequency under various forward sweep rates for the softening beam. Steady state (solid line), $s = 1 \frac{mHz}{s}$ (circles), $s = 2 \frac{mHz}{s}$ (squares), $s = 4 \frac{mHz}{s}$ (diamonds), $s = 6 \frac{mHz}{s}$ (triangles)

As shown in Fig. 3.8, when subjected to a forward frequency sweep, the bandwidth of the response decreases with increasing sweep rate until the parametric response becomes unexcitable above $s = 6 \frac{mHz}{s}$. As the frequency of excitation increases, the response of the harvester follows the stable trivial branch up to the high end of the unstable region where it then abruptly jumps to the stable non-trivial solution branch and continues until the parametric instability ceases beyond 8.75 Hz. Similar

to the hardening beam, as the sweep rate increases, the beam has less time to respond to the instability because of its response time constant. The result is a narrower bandwidth and a lower response peak that shifts toward higher frequencies, which in turn, reduces the power output.

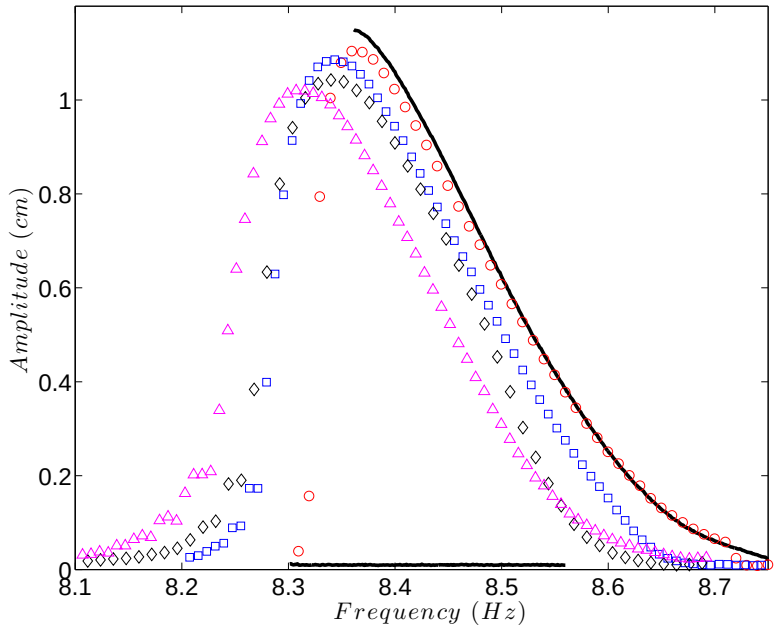

Figure 3.9: Variation of the response amplitude with the excitation frequency under various reverse sweep rates for the softening beam. Steady state (solid line), $s = 1\ \frac{mHz}{s}$ (circles), $s = 4\ \frac{mHz}{s}$ (squares), $s = 6\ \frac{mHz}{s}$ (diamonds), $s = 8\ \frac{mHz}{s}$ (triangles)

Figure 3.9 illustrates the response of the softening beam to a *reverse* frequency sweep. The sweep in this instance is heading toward smaller frequencies, the direction in which the steady state curve bends. As with the hardening beam, for small sweep rates, e.g. $s = 1\ \frac{mHz}{s}$, the time-varying frequency response is very similar to the steady-state response curve. The sweep rate dynamics are on a time-scale that is much slower than the beam dynamics and, therefore, do not interfere with the beam's response. As the sweep rate increases, the response peak shifts to lower

frequencies and the bandwidth increases. For example, when $s = 8\ \frac{mHz}{s}$, the bandwidth increased 35% to 0.520 Hz. Unlike the hardening beam, the parametric instability could not be activated at $s = 14\ \frac{mHz}{s}$, which may be attributed to the larger damping associated with the softening beam.

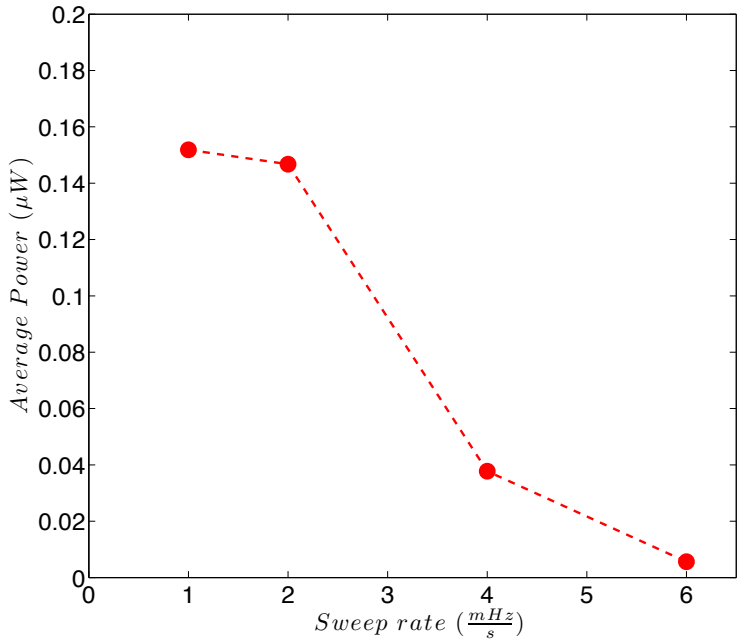

Figure 3.10: Variation of the average output power with the sweep rate for a forward sweep spanning the range between 8.15 Hz and 8.75 Hz. Results are obtained for the softening beam.

Figure 3.11 demonstrates that power output per sweep cycle decreases with increasing sweep rate as expected from the behavior of the response curves. The power output for the forward sweep in Figure 3.10 is significantly less than the power output for the reverse sweep in Fig. 3.11. In general, the *reverse* sweep generates a higher average power than the *forward* sweep. For instance, the *reverse* sweep generates 10 μW of average power per sweep cycle at $s = 6\ \frac{mHz}{s}$, but the *forward* sweep only generates 0.02 μW of power at $s = 6\ \frac{mHz}{s}$. This reaffirms the conclusions drawn previously regarding the hardening beam: a frequency sweep moving in

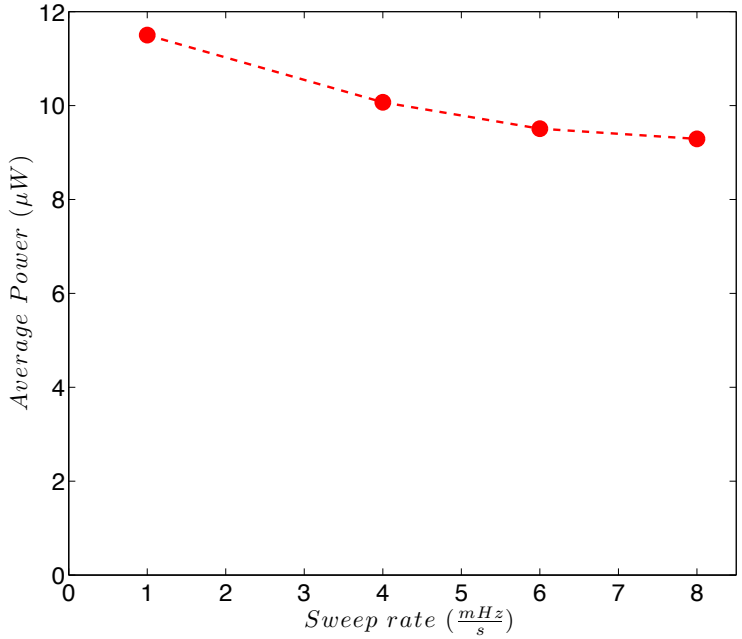

Figure 3.11: Variation of the average output power with the sweep rate for a reverse sweep spanning the range between 8.15 Hz and 8.75 Hz. Results are obtained for the softening beam.

the direction in which the steady-state response curve bends generates significantly more power than a frequency sweep moving in a direction counter to the bend. The general trend of decreasing power with increasing sweep rate is true for a frequency sweep in any direction, but power output is heavily biased in one direction. Naturally, one would want to design a system which capitalizes on this bias. Such a system is the topic of Section 3.3.3.

3.3.3 The Softening-Hardening Hysteretic Harvester

From the previous analysis of *softening* and *hardening* beams under time-varying frequency excitations, it is evident that a softening beam is more efficient in harvesting energy under excitations of decreasing frequency and that a hardening beam is

more efficient for energy harvesting under excitations of increasing frequency. In an effort to capitalize on these non-linear characteristics, we investigate the potential of using both beams simultaneously in one application to harvest energy from an excitation source whose frequency drifts with time around a center frequency. There are few, if any, single fixed-frequency applications for energy harvesting outside of the laboratory. In many applications, the excitation frequency may vary in both directions about a center frequency. For instance, a pump run by a synchronous AC motor will operate at a center frequency of 60 Hz. However, the grid frequency varies slightly and the load on the pump, even at steady state, is not perfectly constant. In such a scenario, it is reasonable to assume that the main component of the pump's vibrations may vary slightly around the 60 Hz center frequency.

Conceptually, to maximize efficiency, a harvester should be designed such that its bandwidth covers the entire excitation bandwidth and that it is capable of harvesting energy in both directions of the frequency sweep. Figure 3.12 illustrates the conceptual voltage response of a harvester capable of harnessing energy from a time-varying frequency spanning the range between ω_{min} and ω_{max}. To achieve this type of voltage response, a harvester would need to consist of one hardening and one softening beam with slightly different fundamental frequencies. $Beam1$ is designed to have a fundamental frequency ω_1 where $\omega_{min} \approx 2\omega_1$ and $Beam2$ will be designed to have a fundamental frequency ω_2 where $\omega_{max} \approx 2\omega_2$. The harvester would operate as follows. Starting at ω_{max}, as the excitation frequency decreases, the steady-state voltage follows line ab. Within this small region, no energy can be harvested because the steady-state voltage is zero. As the frequency decreases further, the voltage follows line bc, which represents the region where $Beam$ 2 is being excited and is harvesting energy from the source. Beyond point c, $Beam$ 2 stops oscillating, and the output voltage drops to point d. Now, as the frequency increases, $Beam$ 1 starts oscillating and harvesting energy following line ef and the process continues.

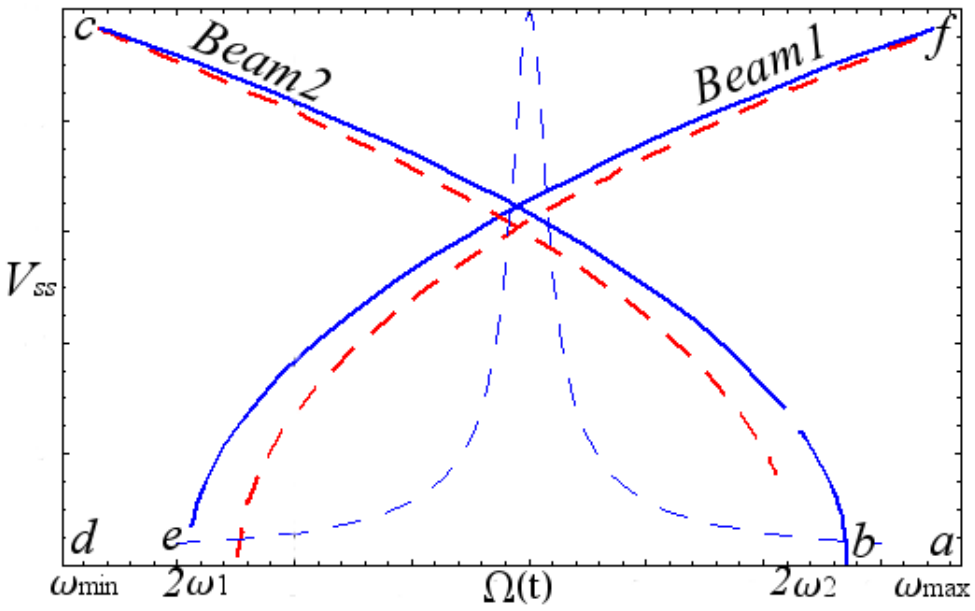

Figure 3.12: Variation of the steady-state output voltage with the excitation frequency for the conceptual SHHH. For the purpose of comparison, thin dashed lines represent the response of the common linear directly-excited cantilever using similar excitation levels.

A harvester of this design would harvest energy in both sweep directions over the entire frequency range, yielding maximum average power. The hardening and softening beams used in these experiments do not have the ideal response curves seen in Fig. 3.12, but they will serve to illustrate the concept. The nature of the steady states curves in Fig. 3.13 means that the center frequency, ω_c, is under-utilized and thus a significant amount of available power is not captured.

Two beams, one softening and one hardening, designed and implemented (see Fig. 3.16 for set-up), in such a manner that their steady-state response curves overlap by a small margin, as in Fig. 3.13, have the potential to harvest energy from both sweep directions. Figure 3.14 demonstrates the harvesting potential of the Softening-Hardening Hysteretic Harvester under a bi-directional time-varying frequency excitation source, with a center frequency of 8.6 Hz, a bandwidth of 0.8 Hz, and a sweep rate of 2 $\frac{mHz}{s}$. Variation of the excitation frequency with time for this

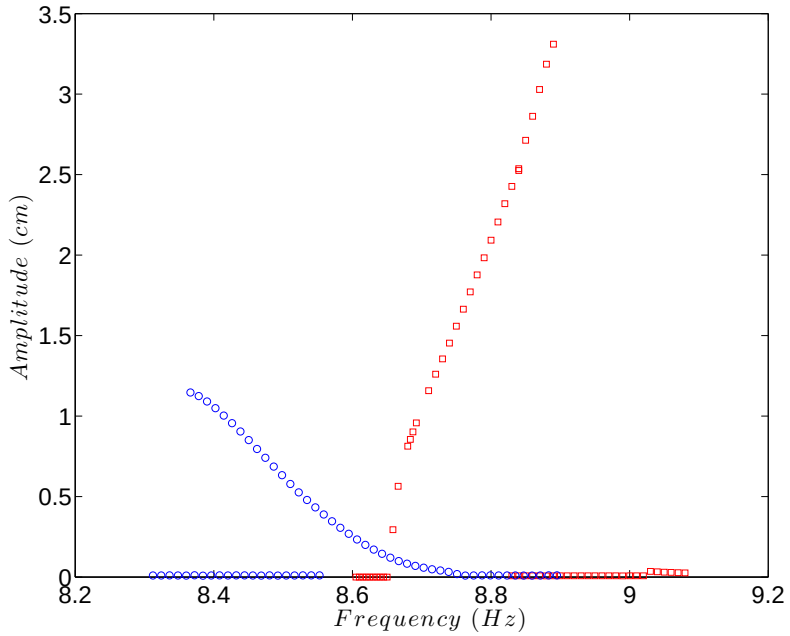

Figure 3.13: Variation of the steady-state response amplitude with the excitation frequency for both the hardening (square), and the softening beam (circle).

experiment is illustrated in Fig. 3.15.

If only a single hardening beam is utilized, the harvester's bandwidth is roughly equivalent to the beam's bandwidth in the forward sweep and almost half the bandwidth during the reverse sweep. As the frequency increases from the end of the excitation bandwidth, 8.2 Hz, the beam does not oscillate up until the excitation frequency reaches 8.65 Hz. The beam follows the non-trivial branch of solutions until oscillations cease to exist at around 8.90 Hz. As the frequency reverses direction at 9.0 Hz, the beam follows the trivial branch of zero oscillations down to about 8.75 Hz where it jumps to the non-trivial branch of solutions and follows that curve down to 8.65 Hz. At this point, the beam stops oscillating and this behavior continues over the rest of the bandwidth. At a sweep rate of 2 $\frac{mHz}{s}$, it was observed

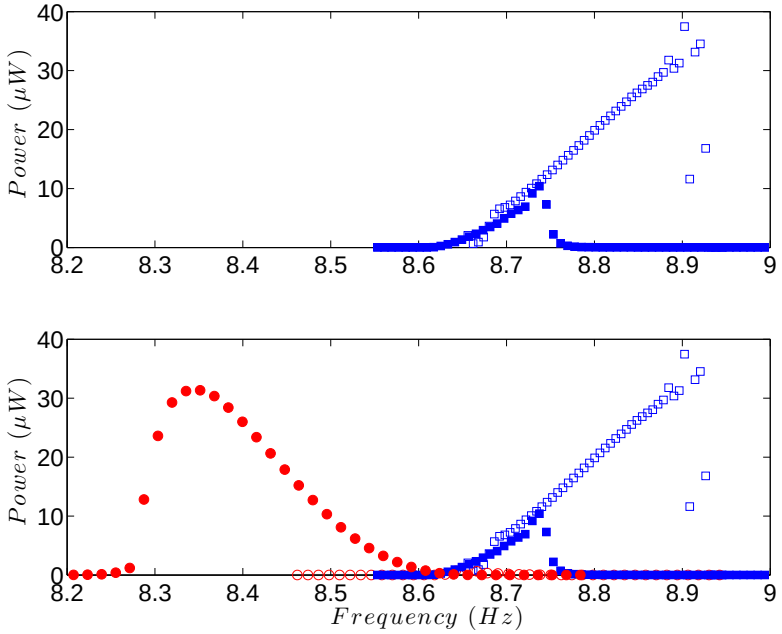

Figure 3.14: Power output at $s = 2\ \frac{mHz}{s}$ for the hardening beam (top) and the hardening beam and the softening beam (bottom). Hardening beam forward sweep (squares), hardening beam reverse sweep (solid squares), softening beam forward sweep (circles), and softening beam reverse sweep (solid circles).

that that a single hardening beam produces about 6.5 μW of average power.

If only a single softening beam is utilized, the harvester's bandwidth is roughly equivalent to the beam's bandwidth in the reverse sweep and almost half the bandwidth during the forward sweep. As the frequency increases from the end of the excitation bandwidth, 8.2 Hz, the beam does not oscillate until the excitation frequency reaches 8.63 Hz. The beam follows the non-trivial branch of solutions until oscillations cease at around 8.75 Hz. When the frequency reverses direction at 9.0 Hz, the beam follows the trivial branch to 8.66 Hz where it jumps to the non-trivial branch of solutions and follows that curve down to 8.24 Hz, where it ceases to oscillate for the remainder of the cycle. At a sweep rate of 2 $\frac{mHz}{s}$, it was observed that that a

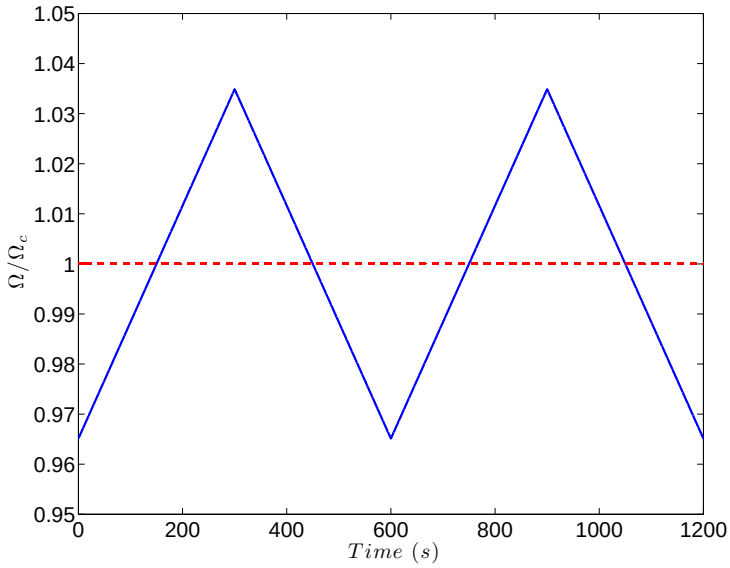

Figure 3.15: Example of a bi-directional, linear-frequency sweep centered at Ω_c with $s = 2\ \frac{mHz}{s}$.

single softening beam produces about 2.8 μW of average power.

When the SHHH is utilized, the harvesting bandwidth increases significantly. Using the same excitation shown in Fig. 3.15, we note the following: As the frequency increases from 8.60 Hz, the forward response curve of the softening excites slightly but then dies out at about 8.77 Hz. The hardening beam on the other hand, starts to oscillate at 8.65 Hz just before the oscillations of the softening beam cease. The hardening beam then continues to harvest energy up to around 8.9 Hz. As the frequency decreases from 8.9 Hz, the hardening beam's reverse response curve excites and then dies out at around 8.65 Hz, where the reverse response curve for the softening beam excites and keeps increasing in amplitude down to around 8.27 Hz. The average power output per cycle using the SHHH at a sweep rate of 2 $\frac{mHz}{s}$ is around 9.3 μW.

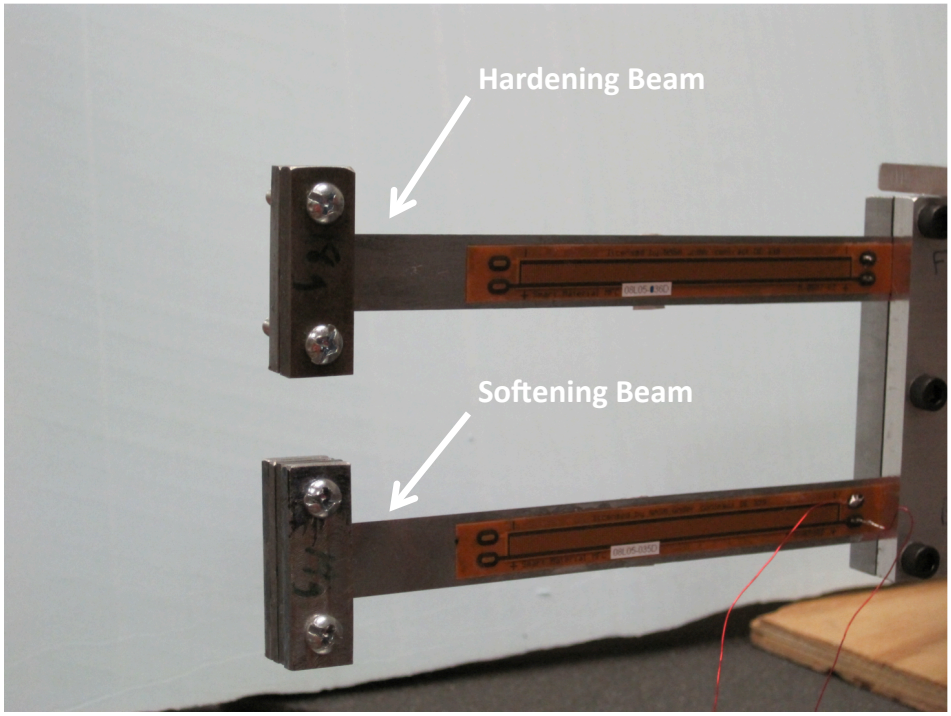

Figure 3.16: Experimental setup showing the concept of the SHHH.

Figure 3.17 shows the average power output per cycle as the bandwidth of oscillation is expanded about the center frequency of 8.60 Hz. Naturally, the SHHH always produces more power. Since the peaks of the response curves in Fig. 3.14 are bi-modally distributed around the center frequency, it follows that when the bandwidth of oscillation is very small, e.g. 0.1 Hz or 0.2 Hz, there will be very small power generation. As the bandwidth of oscillation around the center frequency increases, more of the response curves are included in the bandwidth, yielding more power. At a bandwidth of 0.6 Hz, corresponding to a range of $8.3 - 8.9$ Hz, maximum power is harvested. At this point, the entirety of the response curves for both beams is encompassed by the sweep, yielding maximum power for each beam. Expanding the bandwidth to 0.8 Hz decreases the average power because there is a full 0.1 Hz

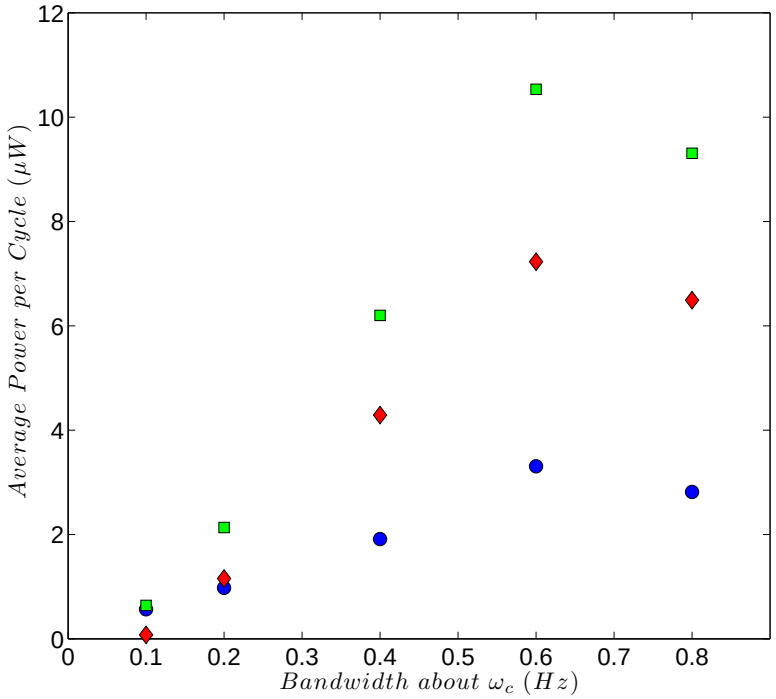

Figure 3.17: Average power output per sweep cycle at different bandwidths of oscillation around a center frequency of $\omega_c = 8.6\ Hz$. Hardening beam (diamonds), softening beam (circles), and the SHHH (squares).

at each end of the sweep cycle where no power is harvested. The implication here is that, if the center frequency and bandwidth of oscillation are known for a given excitation source, then it is possible to design beams with an optimal bandwidth to harvest maximum power, namely a harvesting bandwidth equal to the bandwidth of oscillation about the center frequency.

It is worth noting that the extent to which the parametric resonance curves extend along the frequency domain is greatly influenced by air damping [45]. If an application permitted, placing the beams in a vacuum bell will greatly increase their non-linear response, and hence, their bandwidth.

3.4 Energy Harvesting Under Random Excitations

As mentioned previously, in general, most environmental excitations do not possess well-defined characteristics and are generally either random or have a non-stationary nature. The oscillations of a bridge, for instance, are traditionally random in nature. Their frequency and intensity vary depending on the wind loadings which change unpredictably with atmospheric conditions; and moving vehicles whose number, speed, weight, etc. vary at different times during a given day. Another example would be an engine running at fixed frequency. A fast fourier transform of its vibration shows a bandwidth of frequencies around a dominant frequency that has a sufficient level of forcing for energy harvesting to occur.

To further investigate the behavior of a parametrically-excited harvester under general environmental excitations, we also consider the case of a random Gaussian excitation. To that end, both of the hardening and softening beams were subjected to a band-limited Gaussian noise. The noise was generated by passing a white noise signal through a linear band-pass filter centered at each beam's principle parametric resonance. The variance of the signal was controlled to be within the range of $15 - 16.2\ (\frac{m}{s^2})^2$. The experiments were run for a period of 1000 s and each beam was given a small initial condition at the beginning of each experiment.

Table 3.2: The expected value of the output power under band-limited random excitations of different bandwidths for the hardening beam. $t = 1000\ s$, $\omega_c = 8.875\ Hz$.

Bandwidth	**Mean Power Output**	**Acceleration Variance**
0.25 Hz	6.941 μW	15.051 $(\frac{m}{s^2})^2$
0.50 Hz	2.036 μW	15.082 $(\frac{m}{s^2})^2$
1.00 Hz	0.179 μW	15.849 $(\frac{m}{s^2})^2$
1.50 Hz	0.123 μW	15.199 $(\frac{m}{s^2})^2$

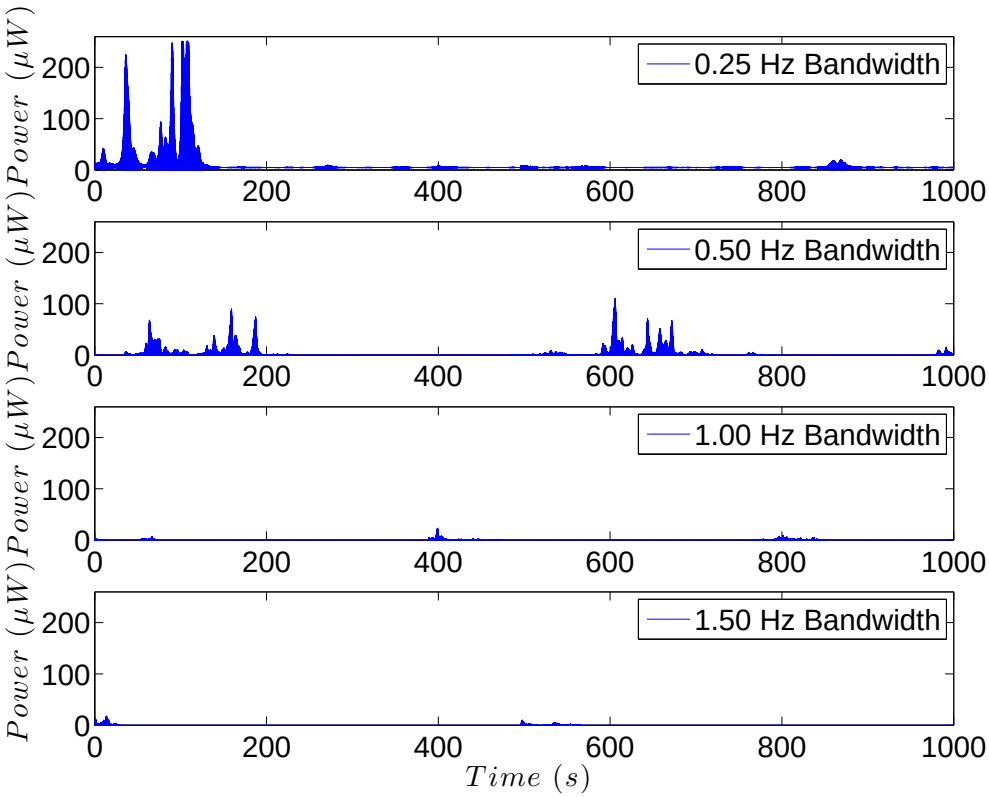

Figure 3.18: Time histories of the instantaneous output power output for the hardening beam when subjected to a band-limited random excitation of a fixed bandwidth.

Table 3.3: The expected value of the output power under band-limited random excitations of different bandwidths for the softening beam. $t = 1000\ s$, $\omega_c = 8.600\ Hz$.

Bandwidth	**Mean Power Output**	**Acceleration Variance**
0.25 Hz	2.302 μW	16.121 $(\frac{m}{s^2})^2$
0.50 Hz	0.252 μW	15.940 $(\frac{m}{s^2})^2$
1.00 Hz	0.024 μW	15.742 $(\frac{m}{s^2})^2$
1.50 Hz	0.005 μW	15.751 $(\frac{m}{s^2})^2$

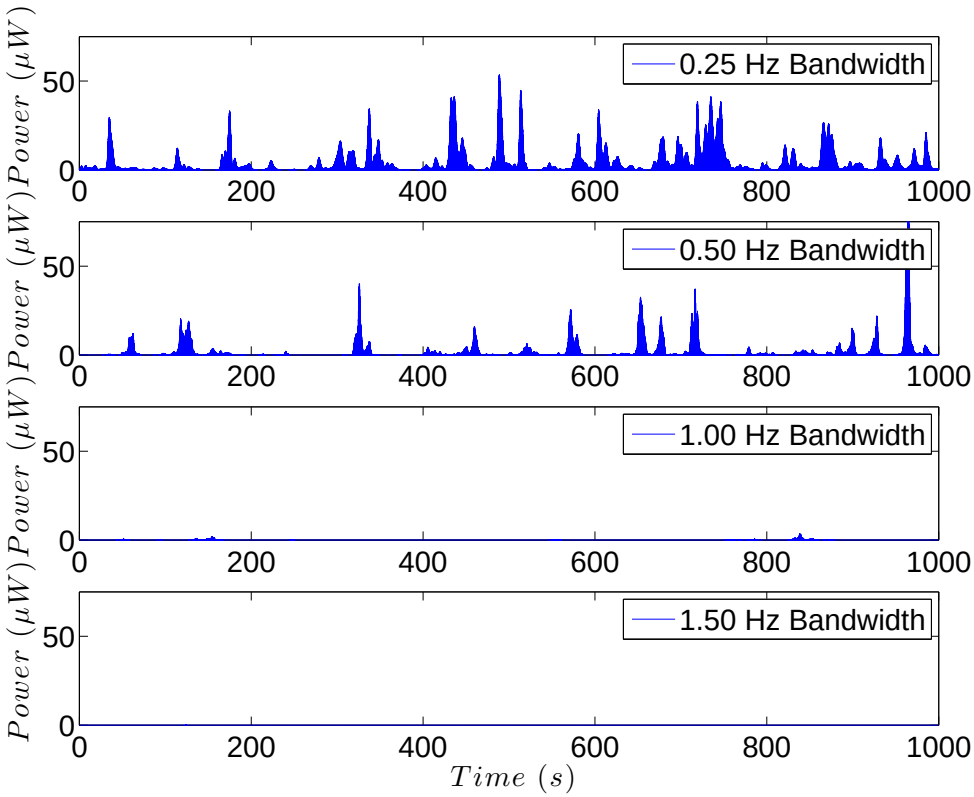

Figure 3.19: Time histories of the instantaneous output power output for the softening beam when subjected to a band-limited random excitation of a fixed bandwidth.

The hardening and softening beams displayed a similar behavior. Initially, the bandwidth was chosen as 0.25 Hz centered around 8.875 Hz for the hardening beam and around 8.600 Hz for the softening beam. For this narrow bandwidth, it was observed that the parametric instability can be excited for significant periods of time. The hardening beam experienced much larger amplitudes for shorter periods of time and produced four times the peak power of the softening beam. Figure 3.19 demonstrates that the softening beam was excited more consistently over the same time period. However, the peak power only crossed the 50 μW range once causing a lower average output power than the hardening beam. Tables 3.2 and 3.3 list the

average power output and acceleration variance at each bandwidth for the hardening and the softening beam, respectively.

As the bandwidth of the random excitations increases, the average power output for the cycle dropped considerably. For the hardening and the softening beams, the change in bandwidth from 0.25 Hz to 0.50 Hz dropped the average power output by 71% and 89%, respectively. The excitation bandwidth was expanded to 1.00 Hz and then to 1.50 Hz; no appreciable power was harvested for these bandwidths using either beam.

Chapter 4

Conclusions and Future Work

4.1 Conclusions

Since this study marks the first investigation of power harvesting via parametrically-excited cantilever beams, our efforts were directed towards obtaining analytical expressions that can be used to estimate the steady-state voltage and harvested power under harmonic excitations. These expressions were obtained using the Method of Multiple Scales and were compared to different experimental findings showing good agreement and reflecting the general trends. Utilizing the resulting expressions, we studied the effect of electromechanical coupling and load resistance on the output voltage and power. We showed that there exist optimal values for the coupling coefficient and load resistance beyond which the harvested power decreases. Furthermore, we demonstrated that the coupling coefficient and load resistance affect the bandwidth of the harvester by shrinking and expanding the range wherein the parametric resonance can be activated. We also demonstrated that to enable energy harvesting using parametric excitations a critical excitation magnitude should always be maintained.

An experimental investigation into parametrically-excited cantilever beams under time-varying frequency excitations was also conducted for both a hardening and a softening beam. It was demonstrated that the bandwidth of the harvester decreases with increasing sweep rate. Also, it was noted that the maximum amplitude of the response during the sweep cycle decreases and shifts in the direction of the sweep. Furthermore, the results show that the power output of the harvester is significantly higher when the sweep is in the direction in which the steady-state frequency-response curves bend. A sweep in the direction of higher frequencies yields more power from a hardening beam than a sweep in the direction of lower frequencies. The reverse is true for the softening beam. We also showed that for slow sweep rates, the sweep dynamics do not interfere with the beam dynamics, so the output is similar to the steady-state response. Conversely, for very high sweep rates, the sweep happens at a much faster time scale than the beam response frequency which does not allow enough time for the beam to respond to the excitation. In such scenarios, no energy can be harvested from a parametrically-excited beam.

In an effort to capitalize on the different nonlinear behaviors of softening and hardening beams, we introduce the concept of the Softening-Hardening Hysteretic Harvester (SHHH). The harvester is designed to scavenge energy efficiently from excitation sources whose frequencies span a range of frequencies in both directions around a center frequency. The optimal SHHH is designed so that the bandwidths of the softening and the hardening beam are equal to the bandwidth of the excitation source. Each beam is excited primarily when the sweep is in the direction that its principle parametric resonance curve bends under steady-state conditions. An introductory experiment showed that this arrangement does produce more power than either a softening or hardening beam alone. However, due to lack of optimization analysis, the experiment suffered from the bi-modal distribution of the frequency response peaks and thus did not prove the full potential of the SHHH arrangement.

Finally, in an effort to duplicate real-world scenarios under which energy harvesting

occurs, both the hardening and the softening beam were subjected to band-limited random Gaussian excitations for a long time that guarantees the stationarity of the ensemble averages. Under narrow bandwidth excitations, e.g. 0.25 Hz, the parametric instability was activated for the length of the experiment. The average power output was low, around 7 μW for the hardening beam. As the bandwidth increased, the power output of both beams dropped considerably until reaching a bandwidth of 1.00 Hz, beyond which no significant power was harvested.

4.2 Future Work

With these results, future efforts should be aimed to compare the effectiveness of direct and parametric excitation for energy harvesting. New studies should investigate scenarios where one approach could be more feasible than the other, or whether some real-life harvesting restrictions could prompt the utilization of one approach but not the other. An interesting area of research could also be directed towards studying harvesters subjected to combinations of direct and parametric excitations.

An analytical solution to the problem of time-varying parametric excitations should be investigated. Having a theoretical solution for this type of excitation will aid in identifying parameters that can be optimized for maximum power generation and also aid in the design of beams that are optimized for non-stationary excitations, such as those usually observed in nature.

The SHHH design should be more thoroughly investigated with a hardening and softening beam that have an ideal bandwidth for harvesting. The optimal power output of a well-designed SHHH system is much greater than the arrangement that was presented in this thesis, which suffered from the bi-modal distribution of its frequency peaks. Further experimental efforts should concentrate on constructing an optimized harvester and studying the effects of air damping on the power output.

Methods for manufacturing beams with predictable hardening or softening behavior also need to be developed. The current method of cutting sheet metal beams with shears and then attaching the piezoelectric element by hand with a commercial super-glue does not always yield consistent results.

Bibliography

[1] H.A. Sodano, D.J. Inman, and G. Park. A Review of Power Harvesting from Vibration using Piezoelectric Materials. *The Shock and Vibration Digest*, 36:197–205, May 2004.

[2] H. Sodano, D. J. Inman, and G.Park. Generation and Storage of Electricity from Power Harvesting Devices. *Journal of Intelligent Material Systems and Structures*, 16:67–75, 2005.

[3] S. Roundy. On the Effectiveness of Vibration-based Energy Harvesting. *Journal of Intelligent Materials and Structures*, 16:809–823, 2005.

[4] A. J. duPlessis, M. J. Huigsloot, and F. D. Discenzo. Resonant Packaged Piezoelectric Power Harvester for Machinery Health Monitoring. In *Proceedings of Smart Structures and Materials Conference, SPIE*, page 5762, San Diego, CA, 2005.

[5] D. J. Inman and B. L. Grisso. Towards Autonomous Sensing. In *Proceedings of Smart Structures and Materials Conference, SPIE*, page 61740T, San Diego, CA, 2006.

[6] R. S. Sanders and M. T. Lee. Implantable Pacemakers. *Proceedings of the IEEE*, 84(3), 1995.

[7] I. D. Capel, H. M. Dorrell, E. P. Spencer, and M. W. Davis. The Amelioration of the Suffering Associated with Spinal Cord Injury with Subperception Transcranial Electrical Stimulation. *Spinal Cord*, 41:109–117, 2003.

[8] G. Renzenbrink and M. J Jzerman. Percutaneous Neuromuscular Electrical Stimulation for Treating Shoulder Pain in Chronic Hemiplegia. Effects on Shoulder Pain and Quality of Life. *Clinical Rehabilitation*, 18:359–365, 2004.

[9] S. Roundy, P.K. Wright, and J.M. Rabaey. A Study of Low Level Vibrations as a Power Source for Wireless Sensor Nodes. *Computer Communications*, 26:1131–1144, 2003.

[10] S. Roundy and P. K. Wright. A Piezoelectric Vibration-Based Generator for Wireless Electronics. *Journal of Intelligent Materials and Structures*, 16:809–823, 2005.

[11] S. W. Arms, C. P. Townsend, D. L. Churchill, G. H. Galbreath, and S. W. Mundell. Power Management for Energy Harvesting Wireless Sensors. In *Proceedings of the Smart Structures and Materials Conference, SPIE*, pages 5763 267–75, San Diego, CA, 2005.

[12] S. P. Gurav, A. Kasyap, M. Sheplak, L. Cattafesta, R. T. Haftka, J. F. L. Goosen, and F. Van Keulen. Uncertainty-based Design Optimization of a Micro Piezoelectric Composite Energy Reclamtation Device. In *Proceedings of the 10th AIAA/ISSSMO Multidisciplinary Analysis and Optimization Conference*, pages 3559–70, 2004.

[13] W. Zhou, W. H. Liao, and W. J. Li. Analysis and Design of a Self-powered Piezoelectric Microaccelerometer. In *Proceedings of the Smart Structures and Materials Conference, SPIE*, pages 5763 233–240, San Diego, CA, 2005.

[14] J. A. Paradiso and T. Starner. Energy Scavenging for Mobile and Wireless Electronics. *IEEE Pervasive Computing*, 4:18–27, 2005.

[15] H.A. Sodano, D.J. Inman, and G. Park. Generation and Storage of Electricity from Power Harvesting Devices. *Journal of Intelligent Material Systems and Structures*, 16:67–75, 2005.

[16] S. Priya, D. Popa, and F. Lewis. Energy Efficient Mobile Wireless Sensor Networks. In *Proceedings of ASME International Mechanical Engineering Congress & Exposition*, Chicago, IL, November 2006.

[17] J.W. Sohn, S.B. Choi, and D.Y. Lee. Am investigation of piezoelectric energy harvesting for MEMS power sources. *Journal of Mechanical Engineering*, 219 Part C, 2005.

[18] S.R. Anton and H.A. Sodano. A Review of Power Harvesting Using Piezoelectric Materials (2003-2006). *Smart Materials and Structures*, 16:1–21, 2007.

[19] N. G. Elvin, N. Lajnef, and A. Elvin. Feasibility of Structural Monitoring with Vibration Powered Sensors. *Smart Materials and Structures*, 15:977–986, 2006.

[20] J.J. Allen and A.J. Smiths. Energy Harvesting EEL. *Journal of Fluids and Structures*, 15:1–12, 2001.

[21] S. Priya, C.-T. Chin, and J. Zahnd. Piezoelectric Windmill: A Novel Solution to Remote Sensing. *Japanese Journal of Applied Physics*, 44:L104–L107, 2005.

[22] J. Granstrom, J. Feenstra, H. A. Sodano, and K. Farinholt. Energy Harvesting from a Backpack Instrumented with Piezoelectric Shoulder Straps. *Smart Materials and Structures*, 16:1810–1820, May 2007.

[23] N.S. Shenck and J.A. Paradiso. Energy Scavenging with Shoe-Mounted Piezoelectrics. *IEEE Micro*, 21:30–41, 2001.

[24] J. Rastegar, R. Murray, C. Pereira, and H.-L. Nguyen. Novel Piezoelectric-Based Energy-Harvesting Power Sources for Gun-Fired Munitions. In Hender-

son B. K. McMickell M. Davis, L., editor, *Industrial and Commercial Applications of Smart Structures Technologies 2007*, volume 6527 of *Proceedings of SPIE*, page 65270Y, San Diego, CA, 2007.

[25] E.O. Torres and G.A. Rincon-Mora. Electrostatic Energy Harvester and Li-Ion Charger Circuit for Micro-Scale Applications. volume 1, pages 65–69, Aug. 2006.

[26] L. Wang and F.G. Yuan. Energy Harvesting by Magnetostrictive Material (MsM) for Powering Wireless Sensors in SHM. In *SPIE Smart Structures and Materials & NDE and Health Monitoring, 14th International Symposium*, volume 15, San Diego, CA, 2007.

[27] W. Huang, B. Wang, R. Yan, S. Cao, L. Weng, and W. Yan. A Numerical Dynamic Model of Giant Magnetostrictive Actuators. In *Proceedings of the 8th International Conference on Electrical Machines and Systems*, volume 1, 1997.

[28] M.E. Staley and A.B. Flatau. Characterization of Energy Harvesting Potential of Terfenol-D and Galfenol. In *Proceedings of the SPIE Smart Structures and Materials 2005: Smart Structures and Integrated Systems*, volume 5764, Bellingham, WA, 2005.

[29] W. Heywang, K. Lubitz, and W. Wersing. *Piezoelectricity: Evolution and Future of a Technology*. Springer, Hoboken, New Jersey, 2008.

[30] N.E. duToit. Modeling and Design of a MEMS Piezoelectric Vibration Energy Harvester. Master's thesis, Massachusets Institute of Technology, Cambridge, MA, May 2005.

[31] N.E. duToit, B.L. Wardle, and S.-G. Kim. Design Considerations for MEMS-Scale Piezoelectric Mechanical Vibration Energy Harvesters. *Integrated Ferroelectrics*, 71:121–160, 2005.

[32] N.E. duToit and B.L. Wardle. Experimental Verification of Models for Microfabricated Piezoelectric Energy Harvesters. *AIAA Journal*, 45(5):1126–1137, May 2007.

[33] K. Nakano, J. Stephen, K. Elliott, and E. Rustighi. A Unified Approach to Optimal Conditions of Power Harvesting Using Electromagnetic and Piezoelectric Transducers. *Smart Materials and Structures*, 16:948–958, 2007.

[34] J. Ajitsaria, S.Y. Cho, and D.J. Kim. Modeling and Analysis of a Bimorph Piezoelectric Cantilever Beam for Voltage Generation. *Smart Materials and Structures*, 16:447–454, 2007.

[35] T.J. Johnson, D. Charnegie, W.W. Clark, M. Buric, and G. Kusic. Energy Harvesting from Mechanical Vibrations Using Piezoelectric Cantilever Beams. In W.W. Clark, M. Ahmadian, and A. Lumsdaine, editors, *Smart Structures and Materials: Damping and Isolation*, volume 6169 of *Proceedings of SPIE*, pages 81–92, San Diego, CA, 2006.

[36] A. Erturk and D.J. Inman. Analytical Modeling of Cantilevered Piezoelectric Harvesters for Transverse and Longitudinal Base Motions. In *Proceedings of 16th AIAA/ASME/AHS Adaptive Structures Conference*, Schaumburg, IL, April 2008.

[37] A. Erturk and D.J. Inman. On Mechanical Modeling of Cantilevered Piezoelectric Vibration Energy Harvesters. *Journal of Intelligent Material Systems and Structures*, 19, 2008.

[38] J. Renno, M. Daqaq, and D. Inman. On the Optimal Energy Harvesting from a Vibration Source. *Journal of Sound and Vibration*, 320:386–405, 2009.

[39] S. Roundy and Y. Zhang. Toward Self-Tuning Adaptive Vibration-Based Micro-Generators. In *Smart Materials, Nano- and Micro-Smart Systems*, Sydney, Australia, 2005.

[40] W. Wu, Y. Chen, B. Lee, J. He, and Y. Peng. Tunable Resonant Frequency Power Harvesting Devices. In *Proceedings of Smart Structures and Materials Conference, SPIE*, page 61690A, San Diego, CA, 2006.

[41] D. Charnegie, C. Mo, A. A. Frederick, and W. Clark. Tunable Piezoelectric Cantilever Beams for Energy Harvesting. In *Proceedings of 2006 ASME International Mechanical Engineering Congress and Exposition*, Chicago, IL, 2007.

[42] V. Challa, M. Prasad, Y. Shi, and F. Fisher. A Vibration Energy Harvesting Device with Bidirectional Resonance Frequency Tunability. *Smart Materials and Structures*, 75:1–10, 2008.

[43] S. M. Shahruz. Design of Mechanical Band-Pass Filters for Energy Scavenging. *Journal of Sound and Vibrations*, 292:987–998, 2006.

[44] M.C. Malkin and C.L. Davis. Multi-Frequency Piezoelectric Energy Harvester. *US Patent 6,858,970*, 2007.

[45] T. J. Anderson, A. H. Nayfeh, and B. Balachandran. Experimental Verification of the Importance of the Nonlinear Curvature in the Response of a Cantilever Beam. *Journal of Vibration and Acoustics*, 118:21–27, 1996.

[46] A. H. Nayfeh and P. F. Pai. Nonlinear Nonplanar Parametric Responses of an Inextensional Beam. *International Journal of Non-linear Mechanics*, 24:139–158, 1989.

[47] S.C. Sinha and A. David. *Encyclopedia of Vibration.* Academic Press, Hoboken, New Jersey, 2001.

[48] W. W. Mumford. Some Notes on the History of Parametric Transducers. *Proceedings of the IRE, May*, pages 848–853, 1960.

[49] M. Faraday. On a Peculiar Class of Acoustical Figures; and on Certain Forms Assumed by a Group of Particles upon Vibrating Elastic Surfaces. *Philosophical Transactions of The Royal Society*, 121:299–318, 1831.

[50] F. Melde. Ueber erregung stehender Wellen eines fadenformeigen Koerpers. *Ann. der Physik u Chemie.*, 109:193–215, 1859.

[51] S. S. Rao. *Vibrations of Continuous Systems*. John Wiley and Sons, Hoboken, New Jersey, 1st edition, 2007.

[52] A.H. Nayfeh and Dean T. Mook. *Nonlinear Oscillations*. John Wiley Interscience, New York, 1st edition, 1973.

[53] A. Erturk and D. Inman. A Distributed Parameter Electromechanical Model for Cantilevered Piezoelectric Energy Harvesters. *Journal of Vibration and Acoustics, Transaction of ASME*, 130:1–14, 2008.

[54] N. G. Stephen. On Energy Harvesting from Ambient Vibration. *Journal of Sound and Vibration*, 293:409–425, 2006.

[55] T. Osorio and M. F. Daqaq. Effect of Bias Conditions on the Optimal Energy Harvesting Using Magnetostrictive Materials. In *Proceedings of the SPIE*, page 69280B, San Diego, CA, 2008.

[56] J. Renno, M. F. Daqaq, J. Farmer, and D. J. Inman. Parameter Optimization of a Vibration-Based Energy Harvester. In *Proceedings of the ASME International Design and Engineering Technical Conference, IDETC2007.*, Las Vegas, NV, 2007.

[57] G. Lesieutre, G. Ottman, and H. Hofmann. Damping as a Result of Piezoelectric Energy Harvesting. *Journal of Sound and Vibration*, 269:991–1001, 2004.

[58] M. F. Daqaq, J. Renno, J. Farmer, and D. J. Inman. Effects of System Parameters and Damping on an Optimal Vibration-Based Energy Harvester. In

Proceedings of the AIAA Structure, Structural Dynamics, and Materials Conference., Honolulu, HI, 2007.

[59] L. D. Zavodney and A. H. Nayfeh. The Non-linear Response of a Slender Beam Carrying a Lumped Mass to a Principal Parametric Excitation: Theory and Experiment. *International Journal of Non-Linear Mechanics*, 24:105–125, 1989.

[60] A. H. Nayfeh. *Perturbation Methods*. John Wiley Interscience, New York, 1st edition, October 1973.

[61] S. Roundy, E. S. Leland, J. Baker, E. Carleton, E. Reilly, E. Lai, B. Otis, J. M. Rabaey, P. K. Wright, and V. Sundararajan. Improving Power Output for Vibration-Based Energy Scavengers. *IEEE Pervasive Computing*, pages 28–36, 2005.

[62] P. Malatkar. *Nonlinear Vibrations of Cantilever Beams and Plates*. PhD thesis, Virginia Polytechnic Institute and State University, Blacksburg, VA, 2003.